ADVANCING EARTH AND SPACE SCIENCES

JGR Atmospheres

RESEARCH ARTICLE

10.1029/2023JD039775

Performance of Common Land Model in Simulating the Land Surface Thermal and Hydrological Processes Over China Improved by Including the Sub-Grid Terrain Solar Radiative Effect

Xindan Zhang[1,2], Anning Huang[3,4], Xianyu Yang[5], Chunlei Gu[3], Shuxin Cai[3], and Jiangxin Luo[3]

[1]Earth System Modeling and Prediction Centre, China Meteorological Administration (CMA), Beijing, China, [2]Key Laboratory of Earth System Modeling and Prediction, China Meteorological Administration (CMA), Beijing, China, [3]School of Atmospheric Sciences, Nanjing University, Nanjing, China, [4]Qinghai Lake Comprehensive Observation Research Station, Chinese Academy of Sciences, Gangcha, China, [5]Plateau Atmosphere and Environment Key Laboratory of Sichuan Province, College of Atmospheric Sciences, Chengdu University of Information Technology, Chengdu, China

Key Points:

- The 3D sub-grid terrain solar radiative effect (STSRE) scheme can much more realistically describe the surface solar radiation over mountainous regions relative to plane-parallel scheme
- Adopting the 3D STSRE scheme clearly improves the CoLM ability in simulating the land surface thermal and hydrological processes over China
- The improvements of CoLM performance induced by the 3D STSRE scheme increase with the terrain complexity increasing

Supporting Information:

Supporting Information may be found in the online version of this article.

Correspondence to:

A. Huang,
anhuang@nju.edu.cn

Citation:

Zhang, X., Huang, A., Yang, X., Gu, C., Cai, S., & Luo, J. (2024). Performance of Common Land Model in simulating the land surface thermal and hydrological processes over China improved by including the sub-grid terrain solar radiative effect. *Journal of Geophysical Research: Atmospheres*, *129*, e2023JD039775. https://doi.org/10.1029/2023JD039775

Received 10 AUG 2023
Accepted 7 DEC 2024

Author Contributions:

Conceptualization: Anning Huang
Data curation: Xindan Zhang, Anning Huang, Chunlei Gu, Shuxin Cai, Jiangxin Luo
Formal analysis: Xindan Zhang, Anning Huang, Xianyu Yang
Investigation: Xindan Zhang, Anning Huang, Xianyu Yang, Chunlei Gu
Methodology: Xindan Zhang, Anning Huang
Resources: Xindan Zhang, Anning Huang
Software: Xindan Zhang, Anning Huang, Chunlei Gu, Shuxin Cai
Supervision: Anning Huang
Validation: Xindan Zhang, Xianyu Yang, Chunlei Gu, Jiangxin Luo
Visualization: Xindan Zhang, Anning Huang

Abstract The sub-grid terrain solar radiative effect (STSRE) significantly affects the heterogeneity of the surface downward solar radiation (SDSR) over mountainous areas, which further exerts remarkable influences on simulations of surface energy budgets and hydrological processes. Given that two thirds of China is mountainous, we have systematically revealed the noticeable STSRE impacts on the performance of the Common Land Model (CoLM) in simulating land surface thermal and hydrological processes over China. Validations indicate that adopting the three dimensional (3D) STSRE scheme clearly improves the CoLM's ability in simulating the land thermal and moist characteristics over China in almost all seasons, and the improvements increase with the terrain complexity increasing. Over the regions with the most rugged terrain, adopting the 3D STSRE scheme can remarkably reduce the overestimated SDSR and thereafter land surface temperature (LST) warm biases in the CoLM with the plane-parallel radiative scheme. The modeled snow cover increases corresponding to the reduced LST with the Taylor score improved the most by 52.84% in summer, and the modeled evapotranspiration (ET) over southeastern Tibet and the Hengduan Mountains is also notably improved in summer. Further analysis indicates that the surface net radiation well corrected by the 3D STSRE scheme firstly reduces the warm biases of LST simulation using the plane-parallel radiative scheme over strong terrain shaded areas, directly leading to the depressed sensible heat flux and ET and more snow accumulation, then the inhibited ET and increased snow accumulation jointly affect the runoff and soil moisture simulations and thereafter latent heat simulation.

Plain Language Summary The landform produces considerable affects on the surface downward solar radiation (SDSR) over regions with rugged terrains, which controls heat and water exchanges between atmosphere and land. Considering that China especially the Tibetan Plateau (TP) owns the most rugged terrains in the world, we introduce a newly developed scheme that much more realistically describes the sub-grid terrain solar radiative effect (STSRE) relative to the plane-parallel radiative scheme in the Common Land Model (CoLM) and indicate its impacts on the model performance. Results show that the CoLM adopting the 3D STSRE scheme could remarkably advance the simulations of land surface energy balance and land thermal and hydrological features. Findings of this study emphasize the necessity of considering the STSRE in simulations of land surface process and hopefully contribute to deepen our understanding of the surface energy budget and improve the land thermal and hydrological simulations over the rugged terrains in China.

1. Introduction

As one of the countries with the most complex terrains in the world, two-thirds of China is mountainous (Figure 1a). Different topographical distributions make the climate in China show notable regional differences (Wu, Huang, et al., 2018; Zhang et al., 2017). Large-scale topography such as Tibetan Plateau (TP) significantly exerts thermal and dynamic effects on the weather and climate through regulating the atmospheric circulation (Wu et al., 2012; Yang et al., 1992; Ye, 1980). Meanwhile, mesoscale and microscale terrains greatly impact the land surface thermal heterogeneity, energy balance, land surface temperature (LST), and local circulation (He, Zhao, et al., 2019; Zhang et al., 2006). One of the most important thermal impacts from the mesoscale and

Writing – original draft: Xindan Zhang, Anning Huang
Writing – review & editing: Xindan Zhang, Anning Huang, Xianyu Yang, Chunlei Gu, Shuxin Cai, Jiangxin Luo

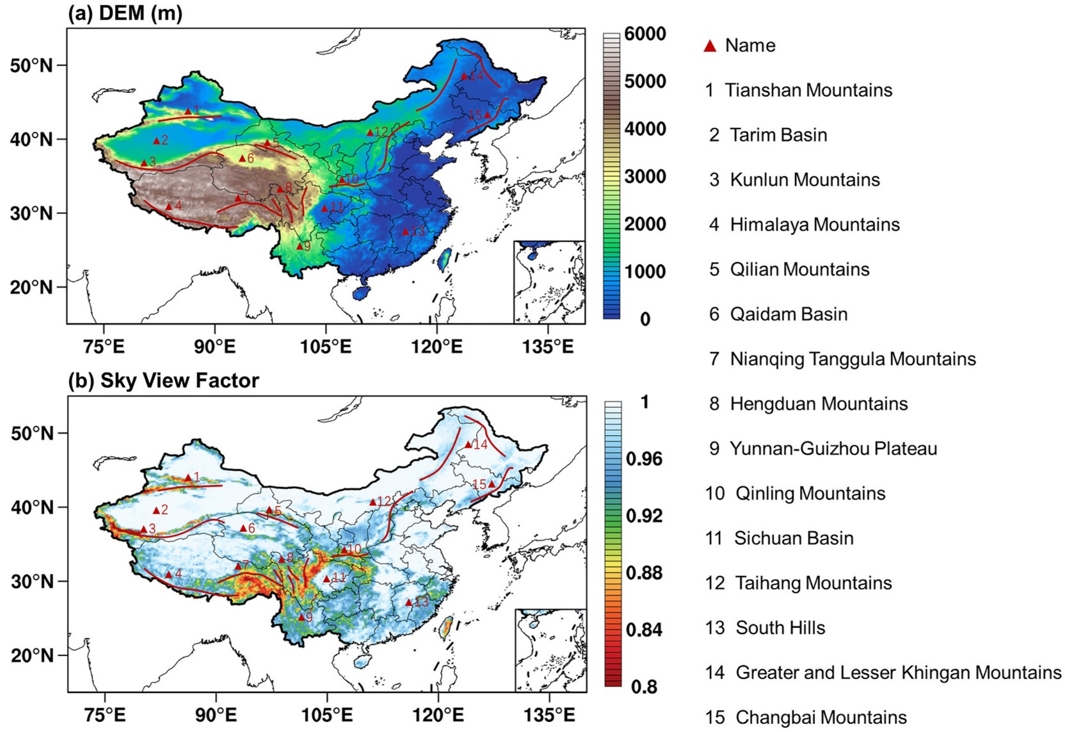

Figure 1. The terrain elevation (a) and sky view factor (b) with a horizontal resolution of 0.1° in China. The major landforms are marked by triangles with names list on the right side.

microscale terrains is the terrain solar radiative effect, which impacts surface downward solar radiation (SDSR) second only to clouds (Ma et al., 2016; Zhang et al., 2022).

The SDSR, as a primary driving component of land surface models (LSMs), obviously affects the accuracy in the simulation of land surface processes such as snowmelt, evapotranspiration (ET), surface energy balance and photosynthesis (L. Chen et al., 2012; Li et al., 1999; Lu et al., 2011; Tang et al., 2006, 2010; Vignola et al., 2007). However, due to many objective limitations such as the heavy computational burden, complicated physical process and poor portability among different models, most of the current numerical models still adopt the plane-parallel radiative transfer scheme that assuming terrains are homogeneous within each model grid, which is inadequate for representing the thermal heterogeneity caused by the reflecting and shading effects of sub-grid topography over complex terrains (Aguilar et al., 2010; Barry, 1992; Y. Chen et al., 2006; Dozier & Frew, 1990; Wang et al., 2005). As the spatial resolution of numerical models increases, the sub-grid terrain solar radiative effects (STSRE) gain essential importance in modeling surface energy budget over the rugged terrains (Lee et al., 2013; Liou et al., 2007; Zhang et al., 2006). For instance, Lee et al. (2013) showed that deviations of the simulated surface net radiation (NR) over the TP induced by the STSRE scheme relative to the plane-parallel radiative transfer scheme could be −10–30, −40–90 and −150–180 W m^{-2} at the model horizontal resolution of 100, 30 and 10 km, respectively, with much larger deviations for the finer model resolution. Considering that China especially the TP is the region with the strongest STSRE in the world which is neglected in most high-resolution LSMs, it is essential to introduce the STSRE scheme in numerical models to further refine the description of land-atmosphere interactions and improve the simulation of key land parameters and surface heat fluxes over complex terrains in China.

A lot of STSRE parameterization schemes (e.g., the radiosity method, the spherical harmonics discrete method and the 3D Monte Carlo method) have been developed over the last three decades (Y. Chen & Liou, 2006; Y. Chen et al., 2005; Dozier & Frew, 1990; Evans, 1998; Fu, 1983; Helbig et al., 2009; Li et al., 1999; Ruiz-Arias et al., 2009, 2010, 2011; Wang et al., 2018; Wu, Wen, et al., 2018) by employing sub-grid topographical parameters such as slope, orientation, sky view factor (SVF) and topographic shading factor (SF) extracted from the Digital Elevation Model (DEM). Accordingly, realistic simulations of key meteorological elements (such as air temperature, precipitation and wind speed) and surface thermal and hydrological processes (including surface heating, snow melting, soil moistening and ET) in numerical models are spurred by the advances in these STSRE schemes (Fan et al., 2019; Gu et al., 2012, 2020, 2022; Hao et al., 2021; Lee et al., 2019; Liou et al., 2013; Muller & Scherer, 2005; Zhang et al., 2018, 2022). Among all these STSRE parameterization schemes, the 3D STSRE schemes more comprehensively deliberate the effects of the 3D structure of neighboring terrains on the SDSR and are the most mature and accurate parameterization scheme in the matter of realistically describing the sub-grid terrain effect (Oliphant et al., 2003; Ruiz-Arias et al., 2010, 2011). To briefly introduce the 3D STSRE scheme, the surface downward diffuse solar radiation is primarily affected by SVF (Dozier & Frew, 1990), which is determined by the obstruction from adjoining landforms and mathematically equivalent to the ratio of the area of the visible sky for an object point to that of an unblocked semisphere on a flat surface. The reflected radiation from adjacent landform is parameterized based on the surface albedo and SVF (Li et al., 2002; Liou et al., 2007). Finally, the most important surface downward direct solar radiation is estimated based on the terrain slope, aspect and the time-variant SF (Dubayah & Rich, 1995; Li et al., 2002). However, the SF is neglected in the idealized 2D STSRE schemes (Arthur et al., 2018; Gu et al., 2020; Hauge & Hole, 2003; Shen & Hu, 2006; Zhang et al., 2006) for lightening the computational burden and avoiding complex integration calculations, thus bringing about nonnegligible overestimation of SDSR during morning and afternoon with lower solar elevation angles and over the regions with high latitudes (He, Smirnova, & Benjamin, 2019).

To overcome the restrictions of previous STSRE schemes, we have recently developed a new 3D STSRE scheme that shares advantages of more reasonable representation of the sub-grid topographical influence and comparatively lower computational cost (Huang et al., 2022; Zhang et al., 2022), and yet successfully coupled it into several numerical models. For example, we have introduced this scheme into the Common Land Model (CoLM) to improve the simulations of surface energy budget, LST, soil thermal and hydrological features through in-situ and regional validations over the Heihe River Basin in TP (Zhang et al., 2022). Adopting this scheme in the Regional Climate Model Version 4 (RegCM4) can also noticeably alleviate summer wet deviations in TP through reducing the biases of SDSR simulation and thus inhibiting the air-heating process near the ground over TP (Gu et al., 2022).

Furthermore, the STSRE schemes mentioned above are generally employed in studies of climate or weather models, which concentrate on the coupling influences between land and atmosphere and the improved simulations of precipitation, air temperature and atmospheric circulations (Liou et al., 2013; Fan et al., 2019; Lee et al., 2019; Gu et al., 2020, 2022). Whereas in coupled models, sub-grid topographical influences on land surface thermal and hydrological processes without complex response to the atmosphere cannot be clearly exhibited. Only a few of the STSRE schemes have been solely used in the LSMs (Hao et al., 2021; Zhang et al., 2018, 2022) to elaborately discuss the separate and direct responses of surface heat fluxes and key surface elements (e.g., the LST, snow cover and ET) to the heterogeneous SDSR. Moreover, aforementioned studies on the sub-grid thermal heterogeneity in China mainly focused on large-scale topographic regions like the TP (Fan et al., 2019; Gu et al., 2020, 2022; Hao et al., 2021; Lee et al., 2019), and paid less attention to much smaller scale topographic regions, for example, the Tianshan Mountains, the Qinling Mountains, the Greater and Lesser Khingan Mountains, the southeast hilly regions and the Taiwan Mountains, etc. As well known that different land cover types and soil parameter conditions can lead to strong differences in responses of key land surface physical processes to the 3D STSRE, such as heat and water transport in ground and vegetation canopy. Thus, it is exigent to pay close attention to the influences of the 3D STSRE on land surface simulations in other complex terrain areas except for the TP of China. Besides, our previous study (Zhang et al., 2022) mainly analyzed the surface energy budget and validated simulations of the soil temperature and moisture in specific small region with large topographical heterogeneities, paying less attention to other important parameters which control the surface heat and water exchanges (like snow cover, ET and runoffs). Possible causes related to the improvement of the CoLM performance in modeling the surface thermal and hydrological exchanges by adopting the 3D STSRE scheme remain to be further studied and revealed.

For this reason, we implement the newly developed 3D STSRE scheme into CoLM and divide the whole China into four research regions with different terrain complexities based on the SVF, to indicate the regional and seasonal impacts in the condition of different sub-grid terrain complexity on the surface heat exchange and land hydrological processes over China, and offer insight into the potential mechanisms of these effects induced by the 3D STSRE scheme in modeling land surface processes, which have not been elaborately studied in previous papers.

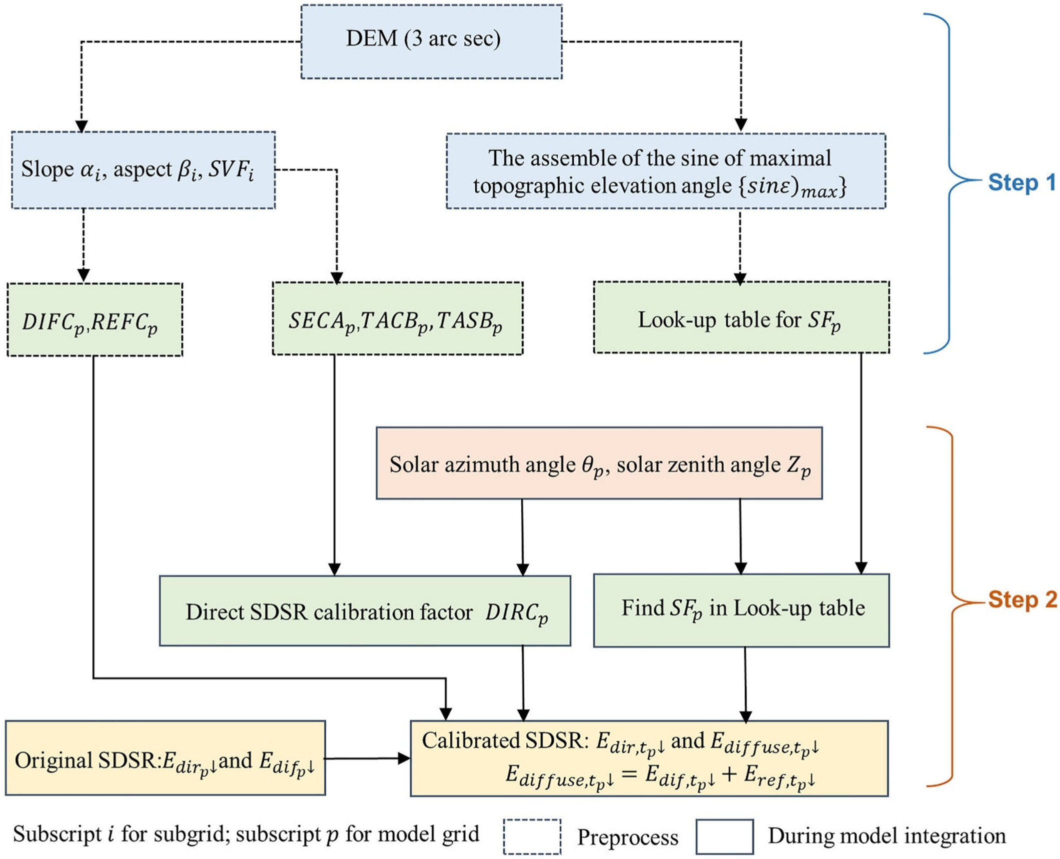

Figure 2. The summary flowchart for coupling the 3D sub-grid terrain solar radiative effect scheme into the CoLM.

Section 2 introduces the CoLM Model, 3D STSRE scheme, data and numerical experimental design. Section 3 evaluates the influences of 3D STSRE scheme on the performance of CoLM over China and indicates the possible mechanisms. The main conclusions and discussions are given in Section 4.

2. Model, 3DSTSRE Scheme, Data, Experimental Design, and Methodology

2.1. Model Description

The CoLM (Dai, 2014; Dai et al., 2003), making use of global soil, vegetation and other key land surface parameter data sets, develops a series of land surface physical schemes in recent years such as the 3D canopy radiative transfer scheme (Yuan et al., 2016), the soil water transfer scheme (Dai et al., 2019) and lake scheme (Qiu et al., 2020) by leveraging the advantages of many prevalent models. Various studies indicate that the CoLM can realistically reproduce the surface heat budget distribution pattern and land surface conditions over arid regions in the northwest of China (Luo et al., 2009; Song et al., 2008; Xin et al., 2006). However, Li et al. (2017) also pointed out that overestimation of the annual LST and underestimation of the annual surface runoff exist in the CoLM over the TP, especially in the southern TP during summer. Besides, the CoLM shows negative bias in snow depth simulation during winter around the high-altitude mountainous areas, such as the south and west slopes of TP, the Hengduan Mountains and Tianshan Mountains. The above unsatisfactory aspects may be partly caused by the original plane-parallel radiative scheme adopted in the CoLM, which neglects the radiative transfer processes affected by the sub-grid topography over mountainous areas and thus overestimates the land surface heating, and such deficiencies are hopeful to be addressed in the following sections through adopting the 3D STSRE scheme in the CoLM Model.

Table 1
List of Symbols

Symbols	Definitions
$SECA_p$	The area weight coefficient for a model grid
$DIRC_p$	The grid-scale topographical correction factor for the direct solar radiation
$TACB_p$, $TASB_p$	The grid-scale factor for the calculation of $DIRC_p$
$DIFC_p$	The grid-scale topographical correction factor for the diffuse solar radiation
$REFC_p$	The grid-scale topographical correction factor for the solar radiation reflected by surrounding terrain
α	The terrain slope
β	The terrain orientation
SVF	The sky view factor
SF	The shading factor
Z	The solar zenith angle
θ	The solar azimuth angle
p	The grid-scale variable
i	The sub-grid scale variable
E_{ac}	The solar constant
a	The surface albedo
$E_{\mathrm{dir}_p\downarrow}$, $E_{\mathrm{dif}_p\downarrow}$	The grid-scale surface downward direct and diffuse solar radiation by the plane-parallel radiative scheme
$E_{\mathrm{dir},t_p\downarrow}$, $E_{\mathrm{dif},t_p\downarrow}$, $E_{\mathrm{ref},t_p\downarrow}$	The grid-scale surface downward direct, diffuse, and reflected solar radiation by the 3D STSRE scheme

2.2. The 3D STSRE Parameterization Scheme

According to the flow chart shown by Figure 2, we introduce the 3D STSRE scheme (Huang et al., 2022) into the CoLM to correct the SDSR components (direct solar radiation $E_{\mathrm{dir}_p\downarrow}$ and diffuse solar radiation $E_{\mathrm{dif}_p\downarrow}$) at plane surface (Equations 1–3), with the grid-scale orographic calibration factors (shown in Table 1) prepared according to Equations 4–10.

Then, we can achieve three components of the topographical influenced SDSR fluxes at each model grid, the surface downward direct solar radiation $E_{\mathrm{dir},t_p\downarrow}$, the diffuse solar radiation $E_{\mathrm{dif},t_p\downarrow}$, and reflected solar radiation from surrounding terrains $E_{\mathrm{ref},t_p\downarrow}$.

$$E_{\mathrm{dir},t_p\downarrow} = \max\left(SF_p \cdot DIRC_p \frac{E_{\mathrm{dir}_p\downarrow}}{\cos Z_p} / SECA_p, 0.0\right) \tag{1}$$

$$E_{\mathrm{dif},t_p\downarrow} = \begin{cases} E_{\mathrm{dif}_p\downarrow}\left[\dfrac{E_{\mathrm{dir},t_p\downarrow}}{E_{ac}} + DIFC_p\left(1 - \dfrac{E_{\mathrm{dir}_p\downarrow}}{E_{ac}}\right)/SECA_p\right], & \text{if } DIRC_p > 0 \\ E_{\mathrm{dif}_p\downarrow}\left[DIFC_p\left(1 - \dfrac{E_{\mathrm{dir}_p\downarrow}}{E_{ac}}\right)/SECA_p\right], & \text{otherwise} \end{cases} \tag{2}$$

$$E_{\mathrm{ref},t_p\downarrow} = \left(E_{\mathrm{dir}_p\downarrow} + E_{\mathrm{dif}_p\downarrow}\right) a_p REFC_p / SECA_p \tag{3}$$

$$DIRC_p = \cos Z_p + TACB_p \sin Z_p \cos \theta_p + TASB_p \sin Z_p \sin \theta_p \tag{4}$$

$$TACB_p = \frac{1}{n}\sum_{i=1}^{i=n} \tan \alpha_i \cos \beta_i \tag{5}$$

$$TASB_p = \frac{1}{n}\sum_{i=1}^{i=n} \tan \alpha_i \sin \beta_i \tag{6}$$

$$SF_p = \langle SF_i \rangle_{i \to p} \tag{7}$$

$$SECA_p = \frac{1}{n} \sum_{i=1}^{i=n} \sec \alpha_i \tag{8}$$

$$DIFC_p = \frac{1}{n} \sum_{i=1}^{i=n} \frac{\sec \alpha_i SVF_i}{2} (1 + \cos \alpha_i) \tag{9}$$

$$REFC_p = \frac{1}{n} \sum_{i=1}^{i=n} \left(\frac{1 + \cos \alpha_i}{2} - SVF_i \right) \sec \alpha_i \tag{10}$$

E_{ac} is the solar constant and a_p is the surface albedo at the pth model grid. Equations 1–3 are derived from the scheme of Dozier and Frew (1990) and Li and Luo (2015) based on the mountain radiation theory. Generally speaking, the surface downward direct solar radiation $E_{\mathrm{dir},t_p\downarrow}$ in Equation 1 is modified from the direct component $E_{\mathrm{dir}_p\downarrow}$ at plane surface mainly by the calibration factor $DIRC_p$ (Equation 4) representing the influences of terrain slopes and orientations and the shading (Equation 7) casted by surrounding terrains. In Equation 2, the direct radiation $E_{\mathrm{dir},t_p\downarrow}$ ($E_{\mathrm{dir}_p\downarrow}$) at terrain (plane) surface and diffuse radiation $E_{\mathrm{dif}_p\downarrow}$ at plane surface together with the calibration factor $DIFC_p$ (Equation 9) which represents the block effect of surrounding terrain, affect the calculation of the slope surface downward diffuse solar radiation $E_{\mathrm{dif},t_p\downarrow}$. Finally in Equation 3, the reflected solar radiation $E_{\mathrm{ref}.t_p\downarrow}$ from surrounding terrains is simplified to the product of the reflected solar radiation from the ground $(E_{\mathrm{dir}_p\downarrow} + E_{\mathrm{dif}_p\downarrow})\, a_p$ and the calibration factor $REFC_p$ (Equation 10) which represents the area of surrounding terrains participating in reflections. Note that all of the 3 solar radiation components are derived from the sub-grid scale upscaled to the grid scale with the area weighted average (Equation 8).

The accuracy of terrain calibration factors is highly dependent on the resolution of the DEM data. In general, the higher the DEM data we used, the smaller the topography can be captured in terrain calibration factors. For example, Dirksen et al. (2019) pointed out that the accuracy of the SVF is highly sensitive to the resolution of DEM data that using finer grid resolution DEM data can acquire more accurate estimation of SVF. Besides, the coarse-grid SVF values averaged from the highest finer resolution still shows the best approximation. Thus in our scheme, the sub-grid scale terrain calibration factors are first computed from the Shuttle Radar Topography Mission (SRTM) global Database v4.1(Jarvis et al., 2008) with the resolution of 3 arc sec (~90 m) to properly capture the small terrains. Then we aggregate the sub-grid terrain factors to 0.1° grid scale to ensure that the sub-grid terrain can be well represented in the CoLM. Figure 3 shows the time-invariant orographic correction factors with the spatial resolution of 0.1°, which are used in the 3D STSRE scheme.

The factor $SECA_p$ (Figure 3a) is the area weight coefficient determined by the aggregation of the secant value of sub-gird terrain slope α_i ($\sec \alpha_i$), the minimum value 1 implies the flat surface. The role of $\sec \alpha_i$ is assigning different weights to sub-grids with various slopes during aggregation to obtain more realistic and representative grid-scale SDSR fluxes in mountainous regions.

The factors $TACB_p$ and $TASB_p$ (Figures 3d and 3e) together with the solar zenith angle Z_p and azimuth angle θ_p decide the value of grid-scale calibration factor of the surface downward direct solar radiation ($DIRC_p$). Whether values of $TACB_p$ and $TASB_p$ are positive or negative depend on the slope orientation, larger absolute values of $TACB_p$ and $TASB_p$ suggest more significant influence of sub-grid terrain. Besides, smaller $DIFC_p$ implies that the topography exerts more impacts on the surface downward diffuse solar radiation, while the larger $REFC_p$ indicates that the grid receives more solar radiation bounces from the surrounding terrains. The time-dependent shading factor SF_p represents the fraction of sub-grids non-shaded by the adjacent terrain along the current solar azimuth given a certain solar zenith angle in a model grid, which is statistically calculated according to the look-up table method of Zhang et al. (2022) and Huang et al. (2022). It comprises of complex terrain shading conditions in the discrete elevation angles along distributed azimuth angles. In this study, we divide the sine of maximal topographic elevation angle ε into 100 levels ($\sin \varepsilon \le 0.01$, $\sin \varepsilon \le 0.02$, …, and $\sin \varepsilon \le 1$) at 240 azimuth directions with equal interval of 1.5° on sub-grids considering the balance between the simulation accuracy and computing efficiency.

Topographical impacts can bring about heterogeneous distribution of solar energy on terrain surface according to Equations 1–3 different from that on the plane surface. However, the radiation that a fine model grid cannot

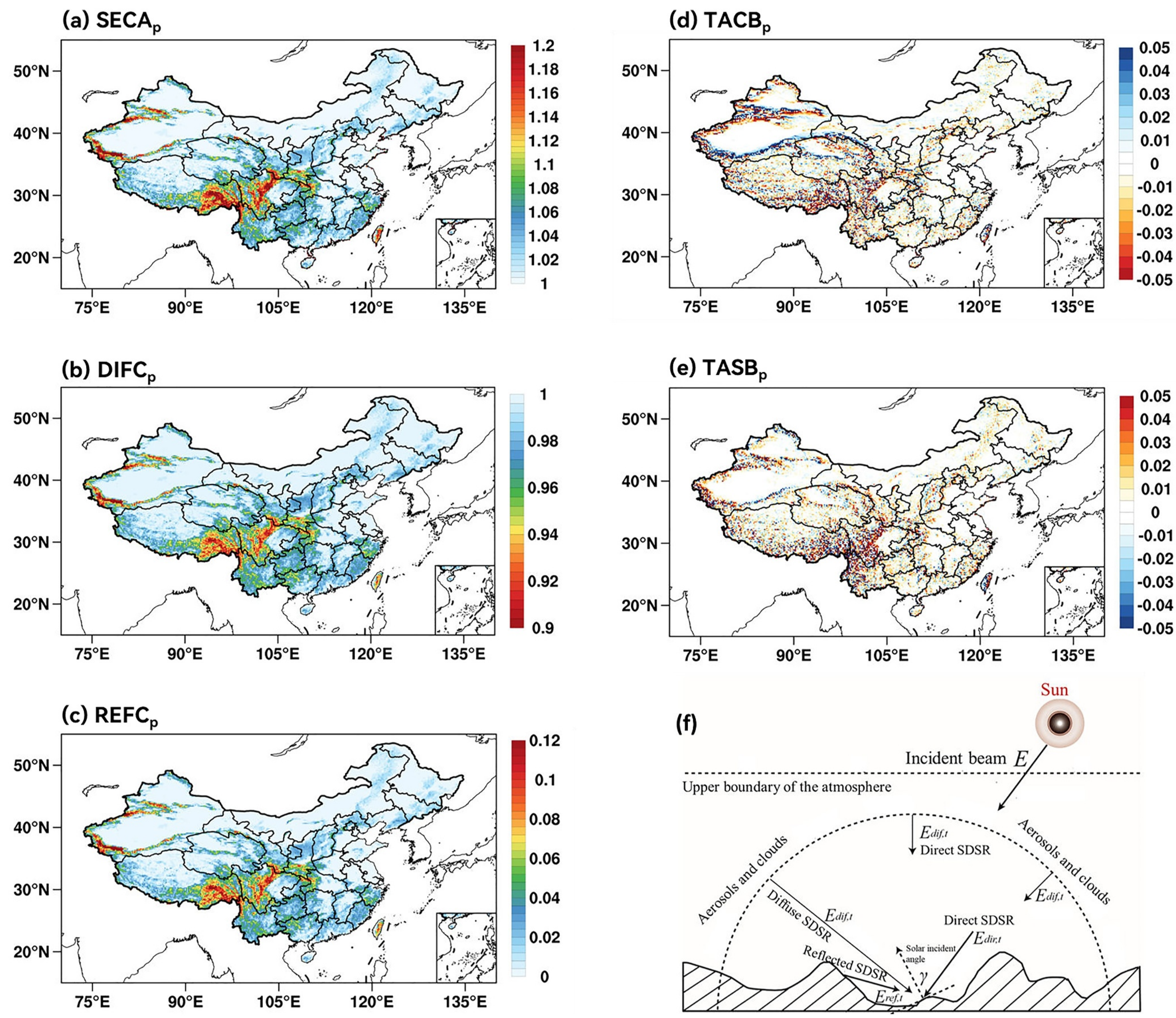

Figure 3. The topographical correction factors: (a) $SECA_p$, (b) $DIFC_p$, (c) $REFC_p$, (d) $TACB_p$, (e) $TASB_p$ for the 3D sub-grid terrain solar radiative effect (STSRE) scheme with a horizontal resolution of 0.1° model grid in China. The schematic diagram for the 3D STSRE scheme is shown by (f).

receive due to terrain obstruction, will right be accepted by its neighboring obstructive model grids. Thus, for an offline LSM, the total solar energy on the land surface does not alter within a coarse scale and just be redistributed between finer-scale model grids (Xian et al., 2023). However, for a coupled model that should consider the energy conservation in the near surface land-air system at each model grid, the upward solar radiation fluxes should be corrected as follows:

$$E_{\mathrm{dir},t_p\uparrow} = E_{\mathrm{dir}_p\downarrow} - E_{\mathrm{dir},t_p\downarrow} \cdot (1 - a_{p,\mathrm{dir}}) \cdot SECA_p \tag{11}$$

$$E_{\mathrm{dif},t_p\uparrow} = E_{\mathrm{dif}_p\downarrow} - (E_{\mathrm{dir},t_p\downarrow} + E_{\mathrm{ref},t_p\downarrow}) \cdot (1 - a_{p,\mathrm{dif}}) \cdot SECA_p \tag{12}$$

where the grid-scale surface albedo $a_{p,\mathrm{dir}}$ for the direct solar radiation is calculated by land model, the $E_{\mathrm{dir},t_p\downarrow}$ is the terrain corrected SDSR at grid scale. The direct radiation flux absorbed by the terrain should be $E_{\mathrm{dir},t_p\downarrow} \cdot (1 - a_{p,\mathrm{dir}})$. Since the downward direct radiation driving the CoLM is $E_{\mathrm{dir}_p\downarrow}$, which is calculated by the plane-parallel radiative transfer scheme, the upward solar radiation flux should be equal to

$E_{\mathrm{dir}_{p}\downarrow} - E_{\mathrm{dir},t_{p}\downarrow} \cdot (1 - a_{p,\mathrm{dir}}) \cdot SECA_{p}$. Similar methods can be used in diffuse fluxes (Equation 12) with slight difference. Since the models do not have the variable of the solar radiation reflected from the surrounding area ($E_{\mathrm{ref},tp\downarrow}$), following the previous studies (Arnold et al., 2006; Hock & Holmgren, 2005; Senkova et al., 2007), we take the solar radiation reflected from the surrounding area ($E_{\mathrm{ref},tp\downarrow}$) as part of the diffuse solar radiation.

2.3. Data

The atmospheric forcing data employed in this study is derived from the three hourly China Meteorological Forcing Data set (CMFD) at a spatial resolution of 0.1° (He et al., 2020; Yang et al., 2010, 2019), which is generated through the hybrid of reanalysis data sets, remote sensing data and in-situ observations from 753 in-situ stations, including seven meteorological parameters in the surface layer (2-m air temperature and specific humidity, surface pressure, precipitation rates, 10-m wind speed, downward shortwave and longwave radiation). Validations against in-situ data exhibit that the CMFD utilizing a larger collection of site observations is better than the Global Land Data Assimilation System (GLDAS) in China (He et al., 2020). However, it should be noted that the SDSR data of CMFD in mountainous areas is not that satisfactory since it does not combined with observations from stations significantly affected by terrains, which is exactly the problem going to be solved by current study.

Furthermore, the validation data sets are listed below:

1. The daily SDSR product from the Global Land Surface Satellite (GLASS) with a spatial resolution of 5 km (Zhang et al., 2014, 2016; Zhang, Wang, et al., 2019; Zhang & Liang, 2018), derived from Moderate Resolution Imaging Spectroradiometer (MODIS) top-of-atmosphere (TOA) reflectance data at 1 km resolution (including the 250 and 500 m resolution bands aggregated to 1 km resolution). The surface elevation correction is added in particular to include the influence of elevation on Rayleigh scattering transmittance by using high resolution DEM data (Kim & Liang, 2010).
2. The SDSR data set with the horizontal resolution of 0.05° by 0.05° and temporal resolution of 10 min for the TP region (22°–45°N, 80°–105°E) during 2016–2018, it is derived from the geostationary satellite Himawari-8 SDSR corrected by terrain effect (Letu et al., 2022), for simplicity, we called this data as H8.
3. The monthly LST product in China with a horizontal resolution of 0.05°, which is generated through the fusion of daily and monthly Terra and Aqua MODIS data and in situ observations (Zhao et al., 2019, 2020).
4. The monthly evapotranspiration data at a spatial resolution of 0.25° provided by the third version of the Global Land Evaporation Amsterdam Model (GLEAM v3, Akash & Petra, 2022; Miralles et al., 2011; Martens et al., 2016, 2017), which is produced by combining the radiation, air temperature and multi-source precipitation reanalysis data, together with the satellite-derived product of soil moisture, vegetation optical depth and snow water equivalent, it shows reasonable agreement with site measurements of 91 eddy-covariance towers across a wide range of ecosystems.
5. The monthly snow cover data at a spatial resolution of 0.05° is aggregated through a combination of the MODIS snow cover data sets (MOD10CM and MYD10CM, Hall & Riggs, 2021a; Hall & Riggs, 2021b) offered by the National Snow and Ice Data Center (NSIDC) with a cloud-free preprocessing.

Generally, the remote sensing data sets show relatively weak performances over complex terrains. Thus, we choose the remote sensing data for validating the SDSR, the LST and snow cover data all have been verified against the observation from meteorological stations in mountainous areas in China. For example, Hu et al. (2013) proposed that compared to the observed SDSR at the Miyun station (in Yanshan Mountains) and the Arou station (in Qilian Mountains) in summer, the GLASS SDSR shows reasonable temporal consistency with the in-situ observations, showing that the relative error in Miyun (Arou) is only about 1.8% (−2.7%). The reconstructed monthly MODIS LST data in China we used has also been assessed in the TP against 2,706 in situ LST records (Zhao et al., 2020). The verification result exhibits the explained variance R^2 of 0.98, the mean absolute error of 1.34°C and the root mean squared error (RMSE) of 1.58°C, indicating that this reconstructed LST data can be suitable to evaluate the model performance in complicated terrain areas. The combined monthly snow cover data at a resolution of 0.05° used in this study is originally aggregated from the MOD10A1and MYD10A1 product with a 500 m resolution. Several comparative analysis and validation of the snow coverage products MOD10A1, MYD10A1 and their combination products, carried out in the northern Xinjiang (Wang et al., 2009; Xie et al., 2009) and the TP (Zhou et al., 2019; Zhou et al., 2019) show reliable performance in the snow classification accuracy over complex terrains. As a summary, though the representativeness of data accuracy analysis for the above remote sensing data over complex terrains still has limitations due to the lack of sufficient in situ observations in mountainous areas, these long time serial and spatial continuous data sets are still reasonable for regional validations due to the sparsity and heterogeneity of observation stations. We have interpolated all these data using the bilinear interpolation method onto the model grid of 0.1° for further model validations.

2.4. Experimental Design

To demonstrate the influences of the 3D STSRE scheme on modeling the land surface energy exchange, land thermal and hydrological processes in China, the control experiment (CTRL) and the sensitivity experiment (SEXP) are conducted by the CoLM with the plane-parallel radiative scheme and the 3D STSRE scheme, respectively. As we mentioned in the introduction section, the STSRE become more significant in modeling surface energy budget over complex terrains with the increasing spatial resolution of numerical models (Lee et al., 2013; Liou et al., 2007; Zhang et al., 2006). Huang et al. (2022) conducted a series of idealized experiment under clear sky condition in 3 sub-regions (the eastern TP, the Great Rift Valley and the parts of the Wai Hinggan Mountains). Comparing with the SDSR explicitly calculated at a resolution of 90 m (aggregated to the corresponding coarse resolution in evaluation), the fraction of model grid that show normalized mean absolute errors within ±1% can reach 76.8%, 84.8%, 88.7%, 91.6%, 93.0%, and 87.1% with the horizontal resolution of 0.025°, 0.05°, 0.1°, 0.2°, 0.4°, and 0.8°, respectively. That is to say, the accuracy of the 3DSTSRE scheme not often increases with finer spatial resolution. Therefore, we decided to conduct experiment at a spatial resolution of 0.1° to balance the accuracy of SDSR simulation and the significance of differences in modeling key parameters of the 3D STSRE scheme. To match the temporal resolution of the CMFD, the model integration time step is set to 3 hours. Offline simulations are performed for 19 years from 1 January 2000 to 31 December 2018 and the model results of the last 9 years are used for validations and analysis. The first 10 years are considered as the model spin-up time to ensure that the surface thermal disturbance signals caused by the 3D STSRE scheme can be entirely delivered from land surface to deeper soil. In validations, we separately discuss the effects of the 3D STSRE scheme in four seasons (winter: from December to February; spring: from March to May; summer: from June to August; autumn: from September to November).

2.5. Methodology

The mean bias error (MBE), relative error (RE) and the RMSE are adopted in this study to evaluate the model errors in quantity (Huang et al., 2016; Kan et al., 2015). These statistical metrics can be expressed as:

$$\mathrm{MBE} = \frac{1}{n}\sum_{i=1}^{n}(S_i - O_i) \tag{13}$$

$$\mathrm{RMSE} = \sqrt{\frac{1}{n}\sum_{i=1}^{n}(S_i - O_i)^2} \tag{14}$$

$$\mathrm{RE} = \frac{S_i - O_i}{O_i} \times 100\% \tag{15}$$

where S_i and O_i respectively indicate the simulated and observed results at the i th point. In addition, to reveal the magnitude and spatial pattern variability of the simulation simultaneously, we used the Taylor score (Ts) proposed by Taylor (2001):

$$Ts = \frac{4(1+R)}{\left(\sigma + \frac{1}{\sigma}\right)^2 (1 + R_0)} \tag{16}$$

where R is the spatial correlation of simulation with observation expressed by Equation 15, and σ demonstrates the resemblance of the spatial variability between two variables (Equation 16). R_0 is the maximum spatial correlation and here is set to 1. Ts varies from 0 to 1 with higher value suggesting better simulating skill.

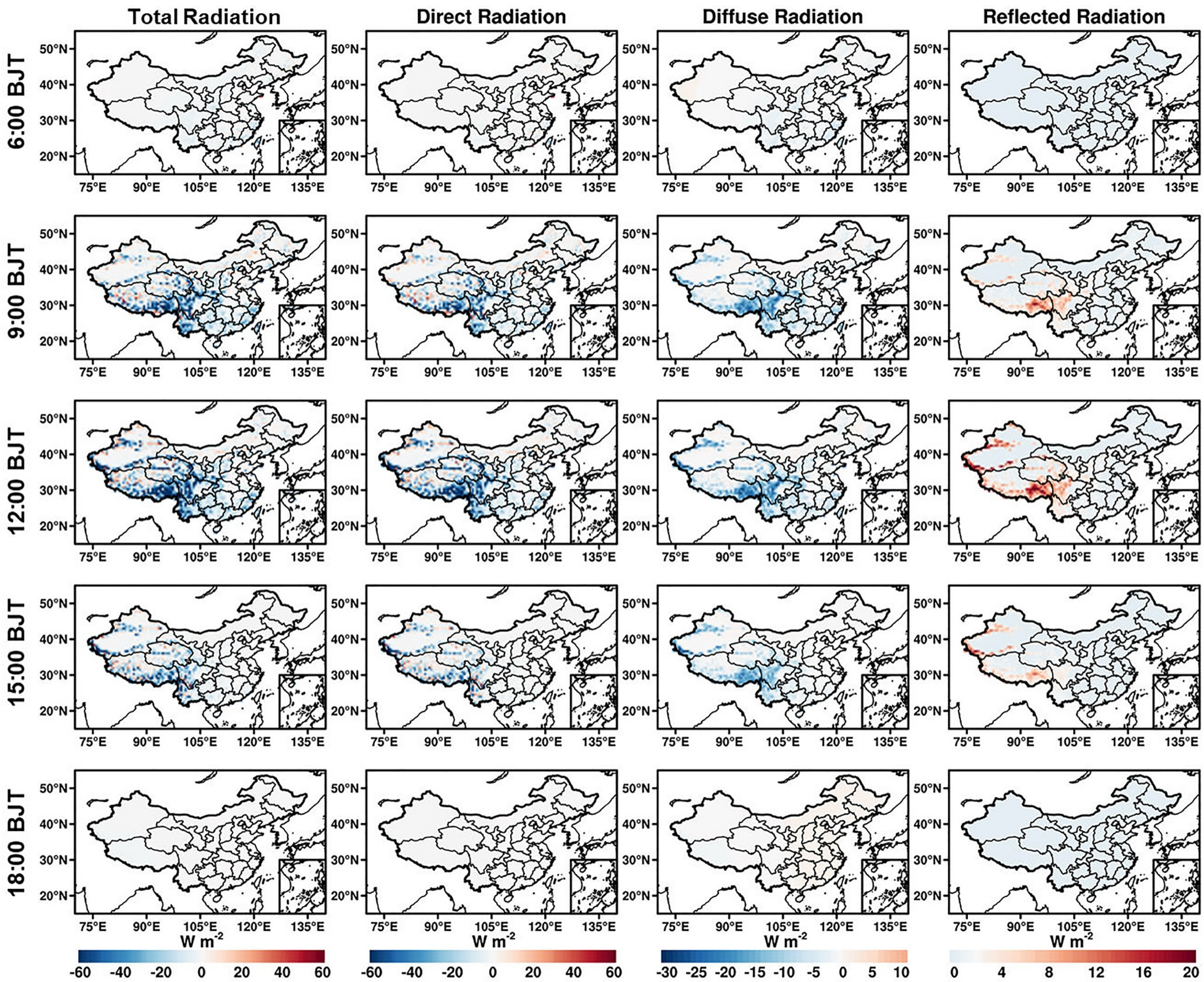

Figure 4. The diurnal variation of the differences in the multiyear mean surface downward total solar radiation flux, direct radiation flux, diffuse radiation flux and surrounding terrain reflected radiation flux during winter between SEXP experiment and CTRL experiment over 2010–2018 from 06:00 to 18:00 BJT.

$$R = \frac{\sum_{i=1}^{n}(\mathrm{S}_i - \overline{S})(\mathrm{O}_i - \overline{O})}{\sqrt{\frac{1}{n}\sum_{i=1}^{n}(S_i - \overline{S})^2 \sum_{i=1}^{n}(O_i - \overline{O})^2}} \tag{17}$$

$$\sigma = \frac{\sqrt{\frac{1}{n}\sum_{i=1}^{n}(S_i - \overline{S})^2}}{\sqrt{\frac{1}{n}\sum_{i=1}^{n}(O_i - \overline{O})^2}} \tag{18}$$

3. Results

3.1. The Influences of 3D STSRE Scheme on SDSR

Figures 4 and 5 show the spatial distribution of diurnal cycles in differences of multiyear mean total SDSR and three components (direct, diffuse and reflected radiation by adjacent terrains) between SEXP and CTRL during winter and summer. Besides, diurnal variations of the above differences over the regions with different SVF and the whole China during winter and summer are also shown in Figure 6. From Figures 4 and 6a-6d we can see that the differences in total SDSR are mainly contributed by those of the surface downward direct solar fluxes,

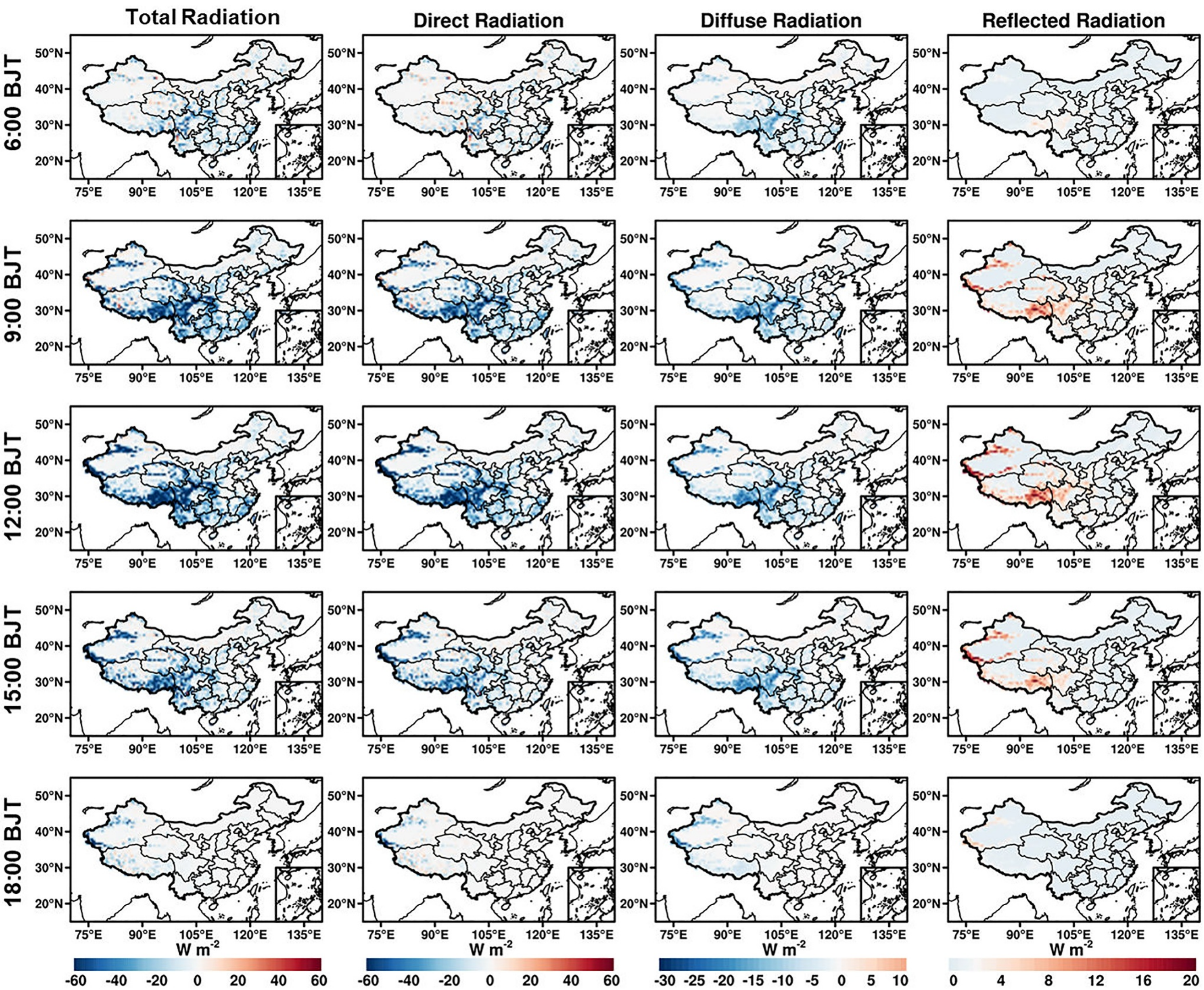

Figure 5. The diurnal variation of the differences in the multiyear mean surface downward total solar radiation flux, direct radiation flux, diffuse radiation flux and surrounding terrain reflected radiation flux during summer between SEXP experiment and CTRL experiment over 2010–2018 from 06:00 to 18:00 BJT.

therefore the spatial distribution and domain averaged diurnal variations of these two fluxes are very consistent and their differences between SEXP and CTRL both decrease with the decline of terrain complexity. When the solar elevation angle peaks at noon, much more obvious negative deviations occur in the regions with strong rugged terrain (SVF < 0.90, Figures 6a and 6b). As shown in Figure 4, the northern slope of the TP maintains daylong negative deviations due to the terrain shading effect. The positive deviations appear in the sunny slopes of mountains, such as the southern foothills of the Altai Mountains, the Tianshan Mountains and the Qilian Mountains, because the south-faced slope can increase the incidence angle of sunlight to increase the surface downward direct solar fluxes while the solar elevation angle becomes lower in winter. The spatial distribution of deviations in surface diffuse solar fluxes is consistent with that of the sky view factor displayed in Figure 1b and the magnitude of diffuse solar radiation deviation is much less intense relative to the direct radiation deviation (Figures 6b and 6c). The deviations of reflected radiation from surrounding terrains account for the smallest proportion of total SDSR compared to the other components (Figure 6d). Relative to the plane-parallel radiative scheme, the 3D STSRE scheme leads to much larger reflected radiation over the regions with rugged terrains, that is, the southeastern TP and Tianshan Mountains. As shown in Figure 5, owing to the increasing solar elevation angle in summer, positive deviations in the modeled total SDSR at sunny slopes, which can last for all the daytime in winter (Figure 5), only occur at 6:00 Beijing Time (BJT) (around sunrise) and 18:00 BJT (around sunset) in

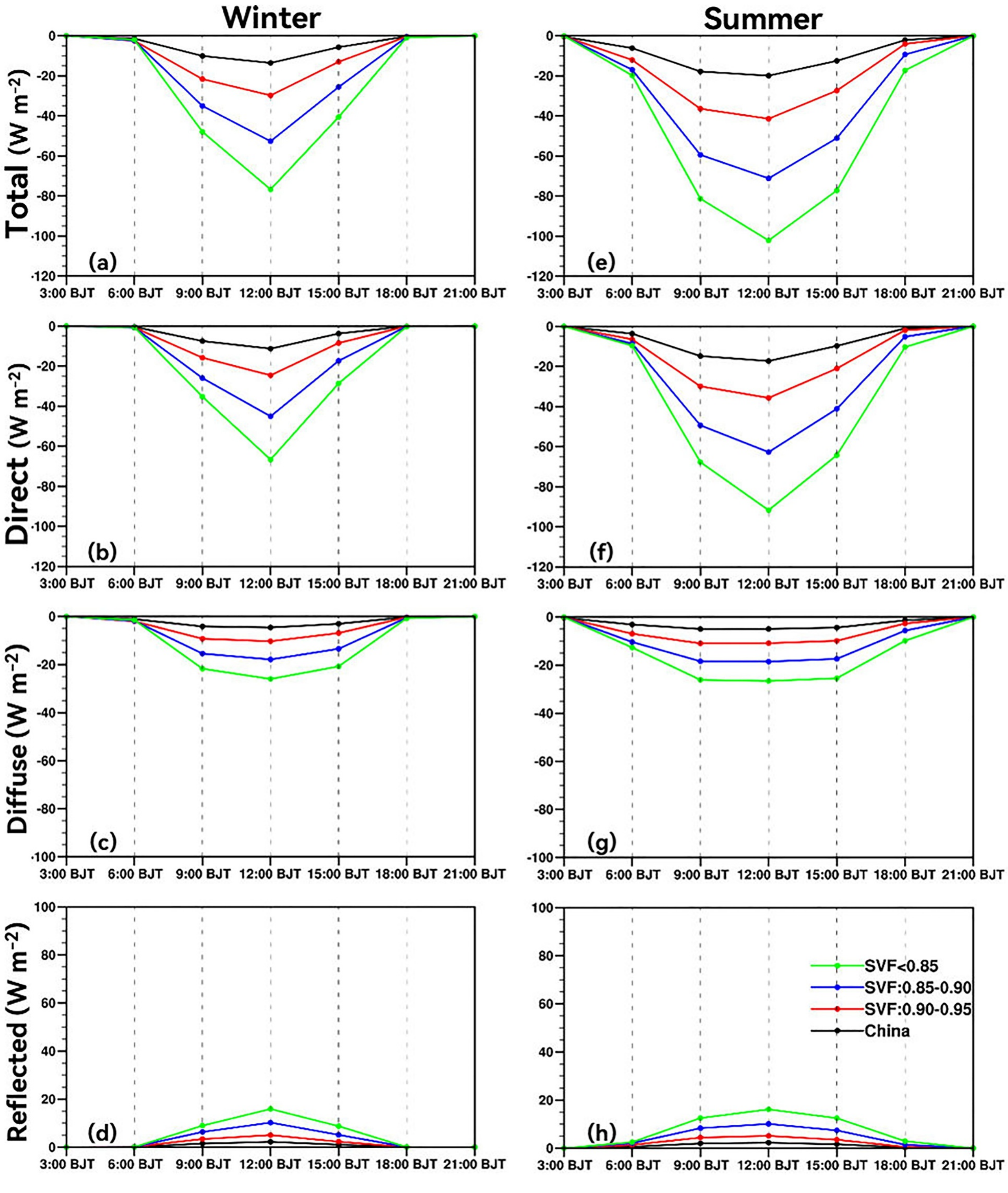

Figure 6. The domain mean diurnal variation of the differences in the multiyear mean surface downward total solar radiation flux (a, e), direct radiation flux (b, f), diffuse radiation flux (c, g) and surrounding terrain reflected radiation flux (d, h) between SEXP and CTRL regionally averaged over the regions with different SVF and the whole China during winter (a–d) and summer (e–g) over 2010–2018.

summer. Between 9:00 BJT and 15:00 BJT in both winter and summer, differences in the direct and diffuse solar fluxes (reflected solar fluxes from neighboring terrains) are dominated by the negative (positive) deviations over rugged terrain areas (Figures 6e–6h).

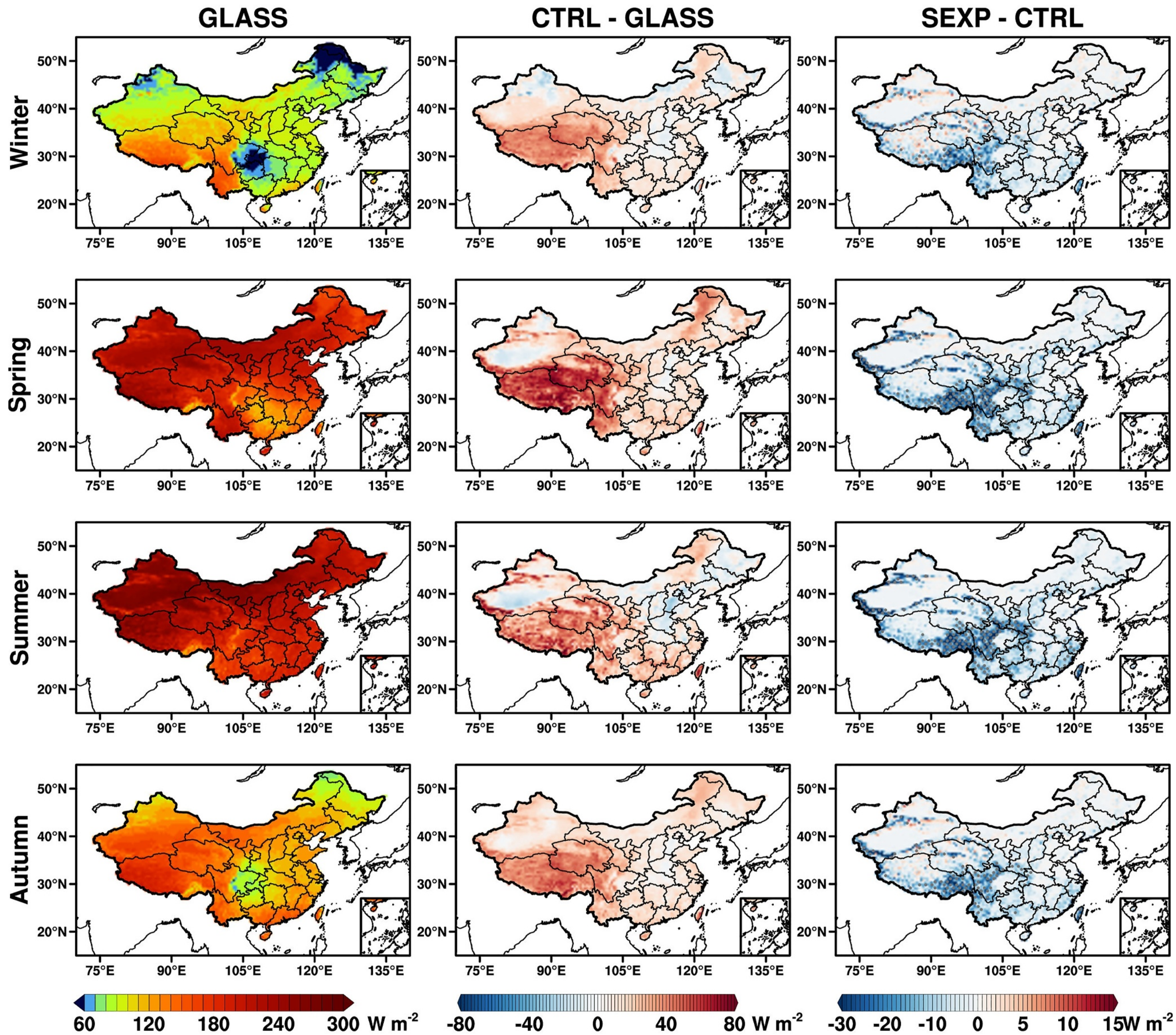

Figure 7. The spatial distribution of seasonal mean GLASS observed surface downward solar radiation (SDSR) from and the differences in SDSR between CTRL simulation and GLASS observation, and between the SEXP simulation and the CTRL simulation over 2010–2018. The gray dots in the right panel indicate the significant level above 95% of t test.

As shown in the left column of Figure 7, the GLASS observed total SDSR shows clear seasonal variations with large (low) intensity in summer (winter). Among the 4 seasons, the largest spatial variability can be noted in winter, during which much higher (lower) total SDSR is located in TP (Sichuan Basin and north part of north-eastern China) with the intensity larger than 120 Wm^{-2} (less than 60 Wm^{-2}). Meanwhile, the total SDSR at the northern slopes of TP, the Qilian Mountains and the Tianshan Mountains is relatively lower than the nearby areas due to the shading effect of surrounding terrains.

From the middle column of Figure 7 and Table 2, in comparison with the GLASS observation, the CTRL experiment adopting the plane-parallel radiative scheme overestimates the total SDSR all year round with a MBE of 15.74 W m^{-2} over most mountainous areas (i.e., TP, Tianshan mountains, Greater Khingan Mountains and the Taiwan Mountains), especially TP and Tianshan where the biases are the most significant in spring and autumn. The SEXP experiment with the 3D STSRE scheme (the right column of Figure 7) can largely reduce approximately 20% positive biases (Table 2) of the total SDSR produced by the CTRL experiment in all seasons.

Table 2
Annual and Seasonal MBE, Root Mean Squared Error and Ts Values of Simulated Surface Downward Solar Radiation in CTRL and SEXP Experiments Relative to GLASS Over the Whole China and Their Relative Changes (RC = (SEXP − CTRL)/CTRL × 100%) Produced by the SEXP Compared to the CTRL

	MBE (W m^{-2})			RMSE (W m^{-2})			Ts		
Season	CTRL	SEXP	RC %	CTRL	SEXP	RC %	CTRL	SEXP	RC %
Annual	15.74	12.41	−21.12	32.05	29.01	−9.48	0.526	0.569	8.17
Winter	11.25	8.28	**−26.38**	36.18	33.13	−8.42	0.344	0.401	**16.57**
Spring	17.40	13.90	−20.09	50.47	47.25	−6.38	0.436	0.443	1.61
Summer	18.19	15.14	−16.73	47.45	44.63	−5.96	0.367	0.370	0.82
Autumn	16.10	12.39	−23.08	31.12	27.60	**−11.30**	0.608	0.675	11.02

Note. Bold values indicate the most significant improvement among all seasons.

Especially in winter, the SDSR simulated by the SEXP shows the most significant improvement with the MBE decreased by 26.4% and the Ts improved by 16.6% (Table 2).

3.2. Validation of Key Land Surface Parameters

LST, snow cover and ET are all key variables for surface water and energy budget calculations. In the LSMs, LST directly controls the calculation of outgoing longwave radiation flux and sensible heat flux, the snow cover affects the estimation of solar radiation and water absorbed by the soil, and ET is the key component of the land surface water cycle and regulates the simulation of latent heat flux. To quantitatively investigate the influences of the 3D STSRE scheme on the ability of CoLM, we evaluated the simulation of the above three critical land surface parameters over China in each season with the model biases (Figures 8–10) and relative improvements in terms of RMSE and Ts (Figures 11c–11h).

3.2.1. Land Surface Temperature

From the left column of Figure 8, the MODIS observed LST over China basically increases gradually from north to south in four seasons, whereas the northwest arid area (especially deserts in Xinjiang and Inner Mongolia) in summer becomes an obvious maximum area of the LST. The LST less than 0°C in all seasons except for summer can be noted in the areas with much higher altitudes, such as the northern and eastern part of the TP including the Kunlun Mountains, the Nianqing Tanggula Mountains and Qilian Mountains.

Compared to the MODIS observations, the LST in most China especially the areas with strongly rugged terrains are obviously overestimated by the CTRL experiment all year round (the middle column of Figure 8) with an annual MBE of 0.98°C (Table 3), similar results are also revealed in the studies of Zheng et al. (2009) and Li et al. (2017), suggesting that the CoLM with the plane-parallel radiative scheme produces warm biases in the modeled LST due to the overestimated SDSR. The warm biases are much more obvious over the areas with the SVF < 0.85 (such as the northern and southeastern part of TP, the Hengduan Mountains, the Qilian Mountains and the Tianshan Mountains) (the middle column of Figure 8) corresponding well to the evidently overestimated SDSR in the CTRL experiment (shown in the middle column of Figure 7). Adopting the 3D STSRE scheme can obviously reduce the warm biases over these mountainous areas in the CTRL experiment (the right column of Figure 8). In Table 3, the MBE values of simulated LST in the SEXP decline about 0.2°C in all seasons compared to the CTRL simulations, resulting in the annual MBE (RMSE) values relatively decreased by 19.5% (3.85%).

3.2.2. Snow Cover

As shown in the left column of Figure 9, the MODIS observed snow cover in the TP mainly sustains at the edge of the plateau where the topography is quite complex (Miao et al., 2022), so that the snow cover over the Kunlun Mountains and the Nianqing Tanggula Mountains maintains more than 40% all year round much larger than that over the central TP (less than 20%). The seasonal snow cover is located outside the TP except for the Tianshan Mountains. Over the northern Xinjiang and northeast China, where the snow cover shows large seasonal variation with the highest snow cover more than 80% in winter among four seasons.

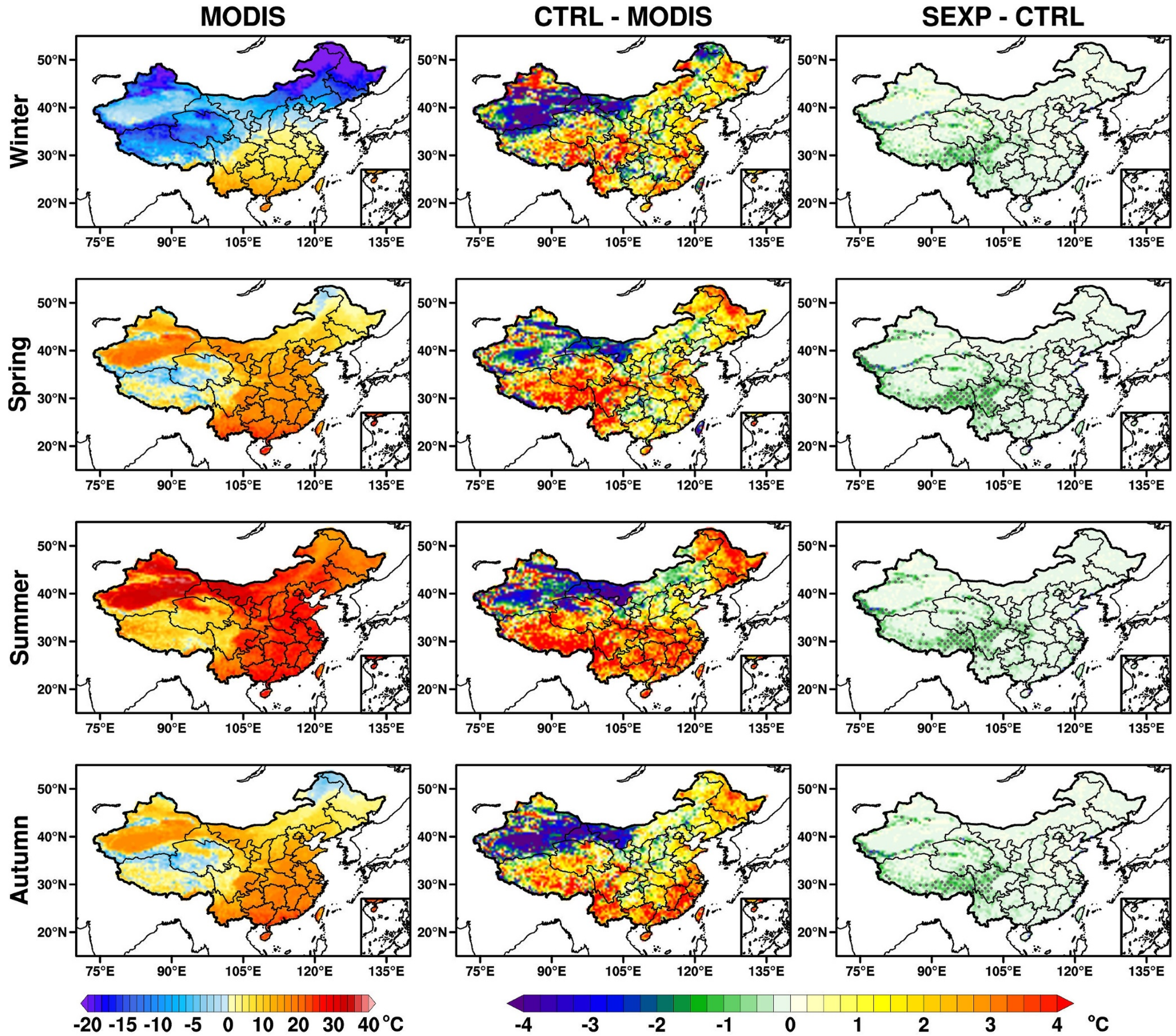

Figure 8. The spatial distribution of seasonal mean MODIS observed land surface temperature (LST) and the LST differences between the CTRL simulation and MODIS observation, and between the SEXP simulation and the CTRL simulation over 2010–2018. The gray dots in the right panel indicate the significant level above 95% of *t* test.

Large deviations in the snow cover between the simulations from the CTRL experiment and observations (the middle column of Figure 9) exist on the TP, varying drastically throughout the year. In winter, the positive bias of snow cover simulation on plateau platform is of most significance, accompanied with overestimation from the south of Tianshan Mountains to Inner Mongolia. However, at the edge of TP, around the Sichuan basin, and around the Greater and Lesser Khingan Mountains and Changbai Mountains, the warm biases of modeled LST (the middle column of Figure 8) caused by the overestimated SDSR increase snow melting, resulting in a significantly underestimated snow coverage, which gradually disappears in low altitude areas owing to the increase of LST and melting snow during spring. The underestimated snow cover on the plateau continues throughout the year only with a relatively smaller magnitude in summer. Taking the STSRE into account, the reduction of LST in the SEXP experiment clearly reduced the positive deviations of the snow cover modeled by the CTRL experiment in the southeastern TP and northern part of China (the right column of Figure 9) with the annual MBE of modeled snow cover in the SEXP deceased by 15.7% and the RMSE (Ts) values decrease (increase) in all seasons (Table 4).

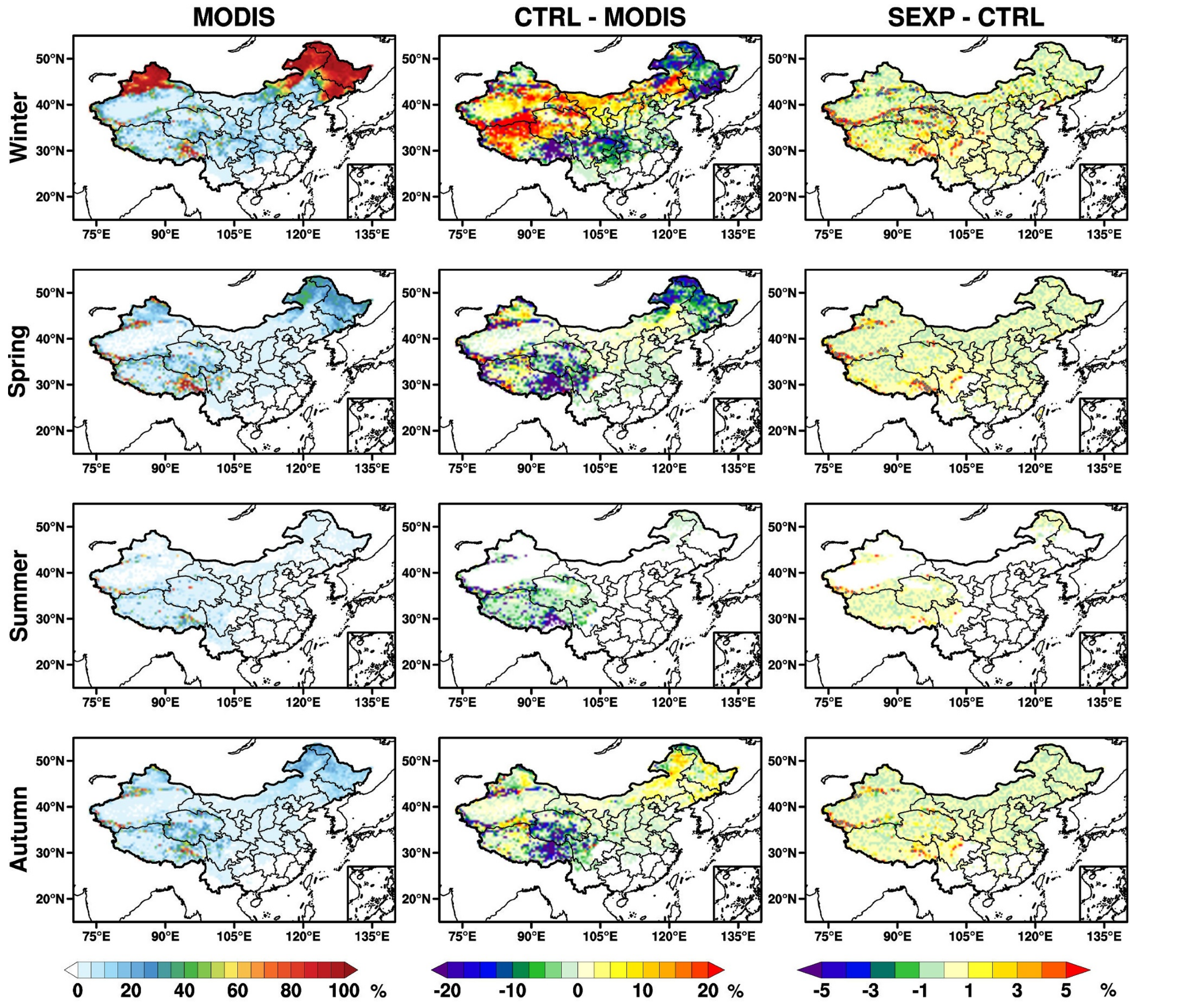

Figure 9. Same as Figure 8, but for snow cover.

3.2.3. Evapotranspiration

In the evaluation of ET, we choose the GLEAM ET product because studies show that it can more realistically reproduce the land surface water balance than other ET products (Martens et al., 2016, 2017). As demonstrated in the left column of Figure 10, the observed ET increases from northwest to southeast, among which the intensity is lower than 20 mm month^{-1} at the Junggar Basin, the Tarim Basin, the Badain Jaran Desert and other northwest arid areas in the whole year. Compared to the ET observations, the CTRL experiment clearly overestimates the ET with much larger biases in summer. However, for the arid and semi-arid regions (excluding TP platforms) with grass land types (Zhang, Liu, et al., 2019), such as the northern slope of TP, the Tianshan Mountains and central Inner Mongolia, the CTRL experiment noticeably underestimates the ET during spring and summer. The CTRL overestimates the ET on the TP platform all year round with much larger overestimation in summer. In addition, in most areas with the land cover type of forest, such as the Yunnan-Guizhou Plateau, southern coastal provinces and the southeastern Tibet, the ET is underestimated by the CTRL experiment throughout the year, suggesting that the CoLM cannot well characterize the evaporation process of canopy precipitation interception for the forest areas with high vegetation canopy height. This surmise is substantiated that the spatial distribution and amplitude

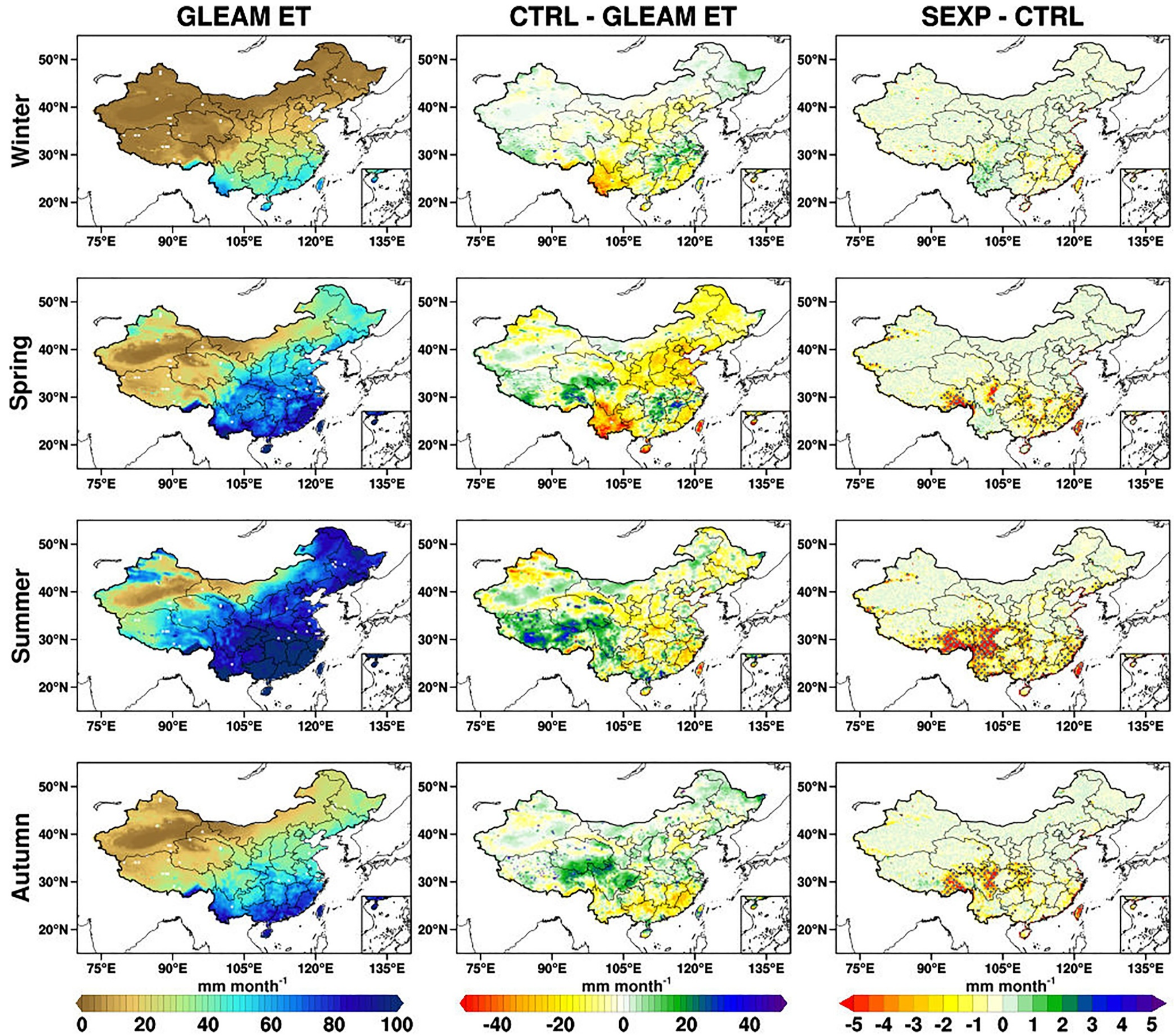

Figure 10. The spatial distribution of seasonal mean ET from GLEAM and ET differences between the CTRL simulation and GLEAM, and between the SEXP simulation and CTRL simulation over 2010–2018. The gray dots in the right panel indicate the significant level above 95% of *t* test.

of the dry biases produced by the CTRL experiment over densely vegetated areas show a good agreement with those of the forest interception loss part in GLEAM product (not shown).

In comparison with the CTRL experiment, the SEXP experiment produced obviously attenuated ET in the southeast Tibet, the Hengduan Mountains, the Taiwan Mountains and other southern coastal regions (the right column of Figure 10). The weakened total SDSR caused by the topographical shading effects notably inhibits the evapotranspiration process and thereafter reduces the positive ET biases in the CTRL experiment. Especially in summer and autumn (Table 5), the 3D STSRE scheme reduces positive ET biases over the whole China by 24.3% and 36.3% respectively, and leads to the reduction (increase) in the RMSE (Ts) of ET simulation at the same time.

3.2.4. The Improvements Induced by the 3D STSRE Scheme

The RMSE (Ts) of the total SDSR in the CTRL experiment over China and the regions with different SVF can be reduced (increased) by ∼10%–40% (∼0–100%) due to the adoption of 3D STSRE scheme (Figures 11a and 11b),

10.1029/2023JD039775

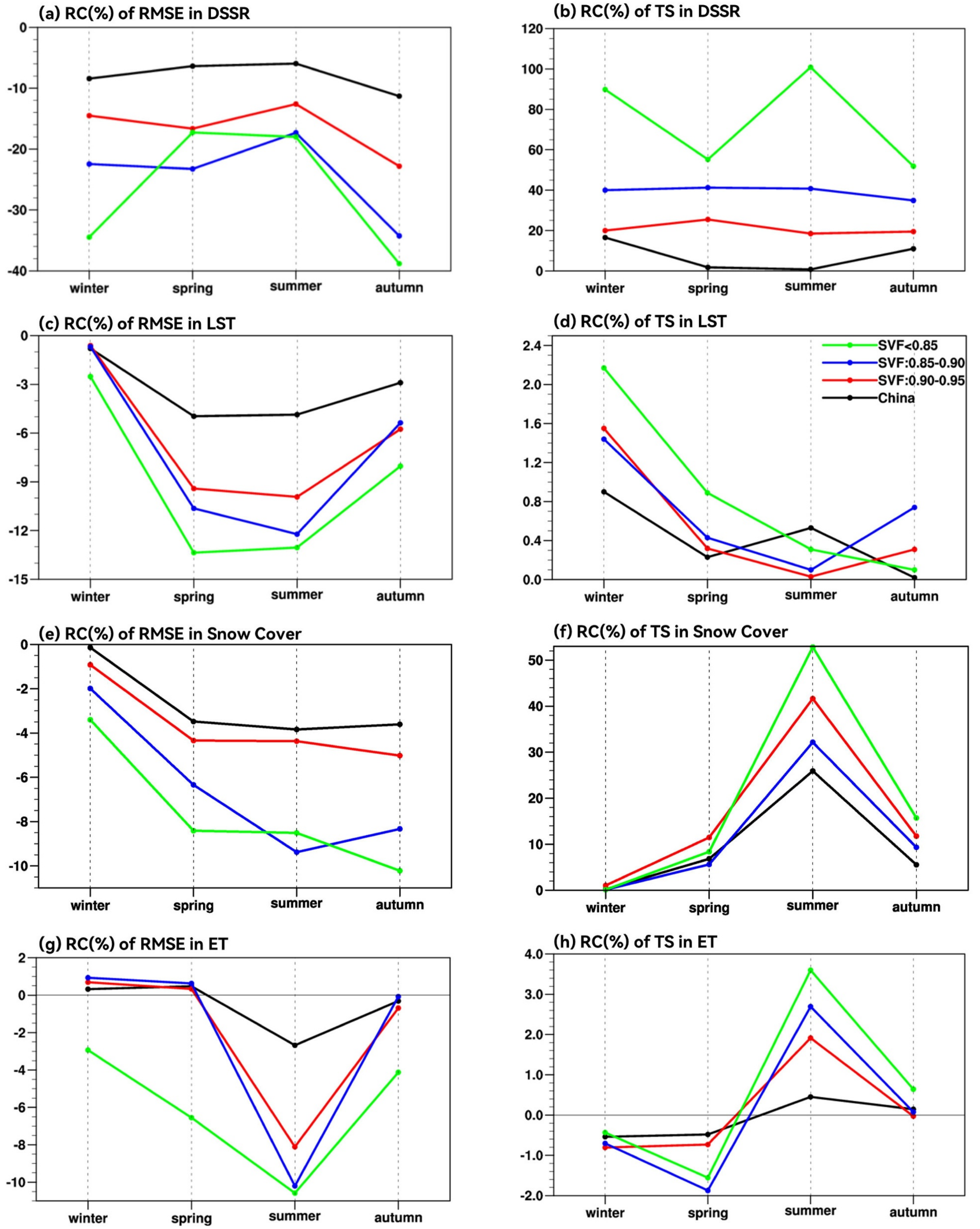

Figure 11. The seasonal mean relative change (RC = (SEXP-CTRL)/CTRL*100%) of the root mean squared error and the Ts of surface downward solar radiation, land surface temperature, snow cover and ET produced by the SEXP experiment compared to the CTRL experiment over the regions with different SVF and the whole China during 2010–2018.

10.1029/2023JD039775

Table 3
Annual and Seasonal MBE, Root Mean Squared Error and Ts Values of Simulated Land Surface Temperature in CTRL and SEXP Experiments Relative to MODIS Over the Whole China and Their Relative Changes (RC = (SEXP − CTRL)/CTRL × 100%) Produced by the SEXP Compared to the CTRL

	MBE (°C)			RMSE (°C)			Ts		
Season	CTRL	SEXP	RC %	CTRL	SEXP	RC %	CTRL	SEXP	RC %
Annual	0.98	0.79	−19.49	2.18	2.10	−3.85	0.970	0.971	0.10
Winter	0.22	0.07	**−70.98**	2.33	2.31	−0.82	0.780	0.787	**0.90**
Spring	1.19	0.97	−18.14	2.17	2.06	**−4.99**	0.860	0.862	0.23
Summer	1.69	1.49	−12.02	2.90	2.76	−4.87	0.950	0.955	0.53
Autumn	0.80	0.62	−22.47	2.24	2.17	−2.91	0.972	0.972	0.00

Note. Bold values indicate the most significant improvement among all seasons.

and the improvements induced by the 3D STSRE scheme enhance with the increased terrain complexity, which is indicated by the SVF with larger (lower) values implying less (more) terrain complexity.

As represented in Figures 11c and 11d, the RMSE (Ts) of the simulated LST in the CTRL experiment over China and the regions with different SVF in the four seasons can be reduced (increased) by ∼1%–14% (∼0–2.2%) due to the adoption of 3D STSRE scheme, similar to the total SDSR, the improvements in the LST simulation induced by the 3D STSRE scheme enhance with the terrain complexity increasing.

Further quantitative analysis indicates that adopting the 3D STSRE scheme can reduce (increase) the RMSE (Ts) of the snow cover simulation in the CTRL experiment by ∼1–10% (0%–50%) over China and the areas with different terrain complexity in all seasons (Figures 11e and 11f).

Figures 11g and 11h further indicate that the RMSE (Ts) of ET produced by the CTRL experiment in summer is obviously reduced (increased) in the SEXP experiment, and the improvements are much more significant in the areas with much lower SVF. However, during winter and spring, the implement of the 3D STSRE scheme progressively weakens the ET in the forest areas, where the ET has already been underestimated by the CTRL experiment. Thus the RMSE of the ET simulation of the CTRL experiment is slightly magnified in the SEXP experiment during winter and spring over almost areas except for the regions with SVF < 0.85 and further leads to slight degradation of Ts when adopting the 3D STSRE scheme. This retrogression is expected to be addressed by more realistically simulating the evaporation process of forest especially the precipitation interception loss in CoLM.

3.3. Possible Causes Related to the Improvement of the CoLM Performance in Modeling the Surface Thermal and Hydrological Exchanges by Adopting the 3D STSRE Scheme

Figure 12 displays the spatial patterns of multiyear mean surface downward NR (downward net solar radiation minus upward net longwave radiation), sensible heat (SH, positive in the upward direction) and latent heat (LH,

Table 4
Annual and Seasonal MBE, Root Mean Squared Error and Ts Values of Simulated Snow Cover in CTRL and SEXP Experiments Relative to MODIS Over the Whole China and Their Relative Changes (RC = (SEXP − CTRL)/CTRL × 100%) Produced by the SEXP Compared to the CTRL

	MBE (%)			RMSE (%)			Ts		
Season	CTRL	SEXP	RC %	CTRL	SEXP	RC %	CTRL	SEXP	RC %
Annual	−1.99	−1.67	−15.72	5.16	5.01	−2.87	0.859	0.879	2.33
Winter	0.80	1.34	66.83	11.22	11.20	−0.14	0.932	0.934	0.21
Spring	−5.26	−4.87	−7.29	6.98	6.74	−3.48	0.697	0.745	6.89
Summer	−5.83	−5.46	−6.21	6.19	5.95	**−3.84**	0.429	0.541	**26.11**
Autumn	−2.03	−1.74	**−14.29**	4.58	4.41	−3.63	0.766	0.808	5.48

Note. Bold values indicate the most significant improvement among all seasons.

Table 5
Annual and Seasonal MBE, Root Mean Squared Error and Ts Values of Simulated ET in CTRL and SEXP Experiments Relative to GLEAM Over the Whole China and Their Relative Changes (RC = (SEXP − CTRL)/CTRL × 100%) Produced by the SEXP Compared to the CTRL

	MBE (mm month^{-1})			RMSE (mm month^{-1})			Ts		
Season	CTRL	SEXP	RC %	CTRL	SEXP	RC %	CTRL	SEXP	RC %
Annual	−4.31	−5.86	35.95	8.10	8.37	3.36	0.961	0.956	−0.52
Winter	−14.64	−15.81	8.05	8.20	8.20	0.32	0.904	0.899	−0.55
Spring	−15.66	−16.97	8.36	13.69	13.84	0.48	0.917	0.913	−0.48
Summer	7.50	5.68	−24.32	10.12	9.85	**−2.68**	0.921	0.925	**0.45**
Autumn	4.62	2.94	**−36.33**	6.13	6.11	−0.33	0.946	0.948	0.21

Note. Bold values indicate the most significant improvement among all seasons.

positive in the upward direction) in the CTRL experiment and their differences between SEXP and CTRL during winter and summer. In winter, due to the reflection of snow and small SDSR, the NR simulated by the CTRL experiment is negative in the areas north of 40°N and positive in the southern TP, the Hengduan Mountains and other high altitude areas, as well as lower latitude areas (Figure 12a). In summer, the NR are positive in the whole China and prominently higher in the central and western parts of TP and southeastern coastal areas (Figure 12g). The spatial distribution of SH and LH fluxes simulated by the CTRL experiment mostly depends on the distribution of arid and humid regions (Figures 12b, 12c, 12h and 12j). In the arid and semi-arid areas, the majority of NR returns to the atmosphere in the form of the SH (Figures 12a, 12b, 12g and 12h). While in the humid and semi humid areas, the surface NR is mainly balanced by the LH (Figures 12a–12c, 12g and 12i). As indicated by Figures 12d and 12j, the spatial distribution of differences in the modeled surface NR between two experiments is in accordance with that of SDSR differences (right column of Figure 7).

The 3D STSRE tends to reduce the NR over the complex terrain areas by more than 10 W m^{-2} during summer and winter with relatively larger intensity of reduction in summer. Meanwhile, relatively obvious positive deviations in winter (Figure 12d) are distributed consistently with the positive deviations in SDSR (Figure 7) on the sunlit slopes of alpine mountains. Hence, differences in the NR further affect the LST simulation (Figure 8), further leading to the deviations of modeled SH (Figures 12e and 12k). Meanwhile, the differences of modeled LH

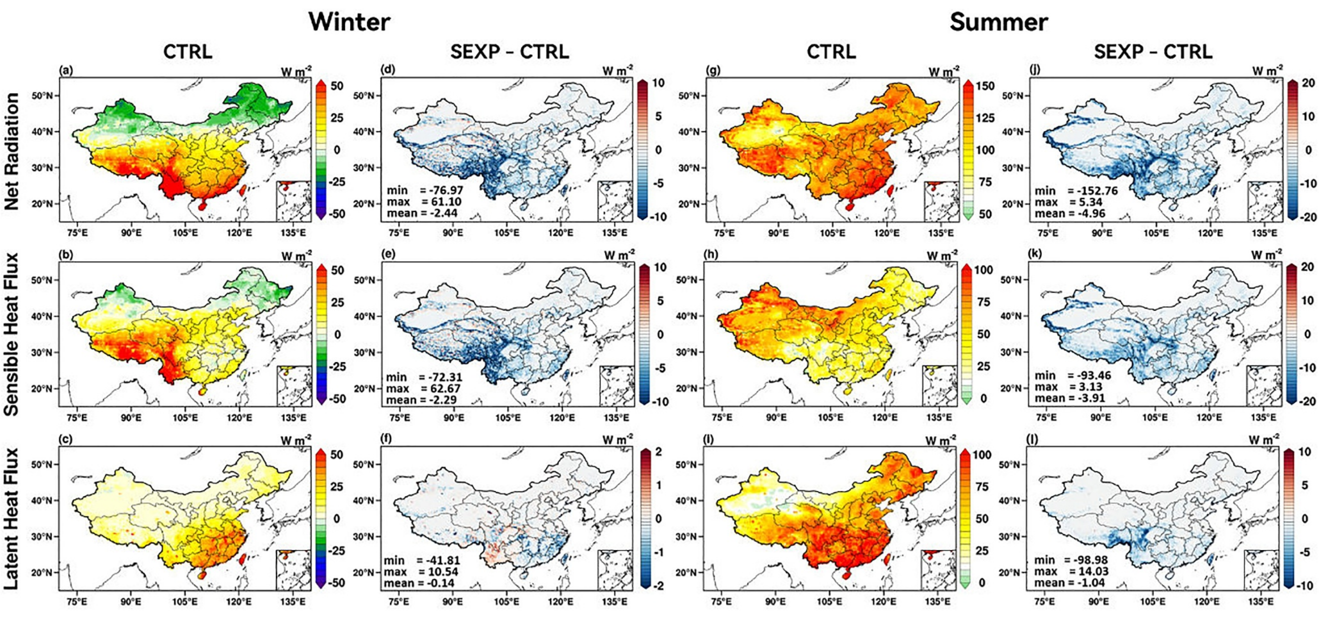

Figure 12. The multiyear mean surface NR, SH and LH simulated by the CTRL experiment and their differences between the SEXP simulation and CTRL simulation in winter and summer over 2010–2018 with extremums and mean values of differences listed upon.

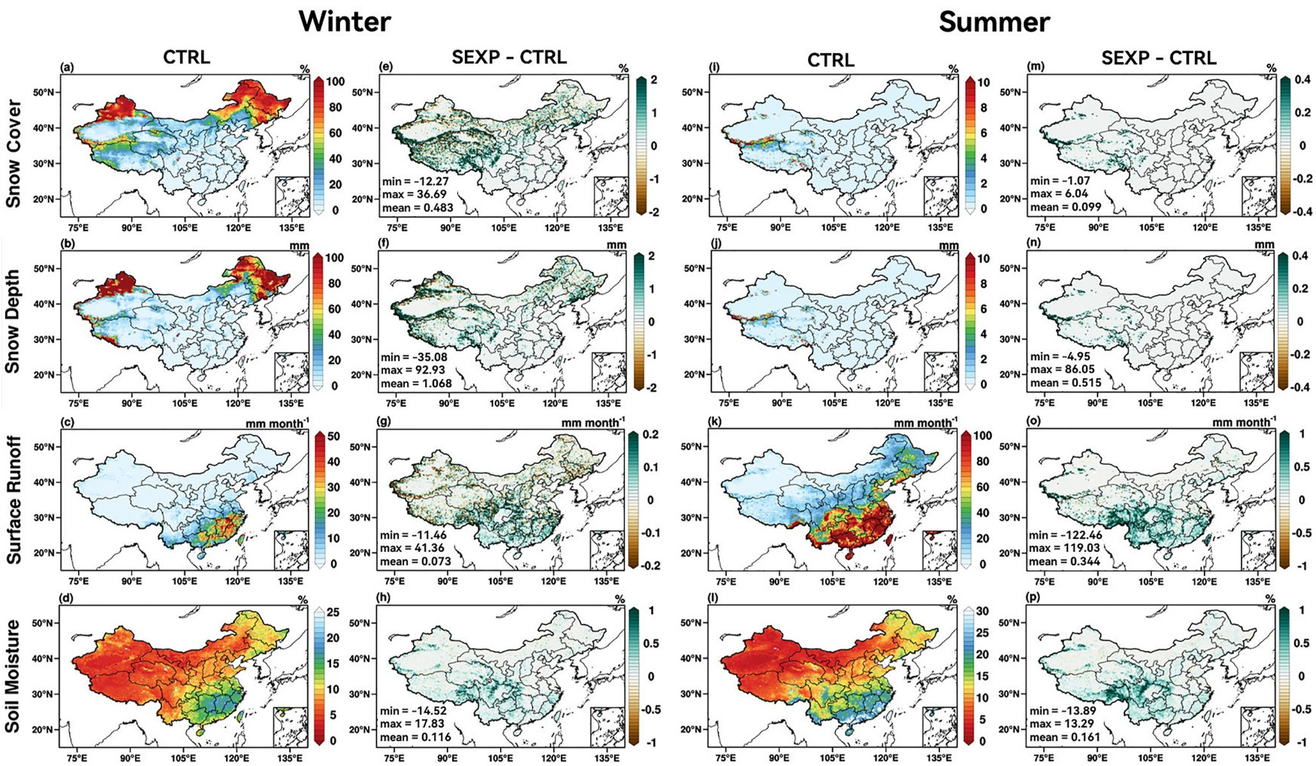

Figure 13. The multiyear mean snow cover, snow depth, surface runoff and surface soil moisture of 0–10 cm soil layers simulated by the CTRL and their differences between the SEXP simulation and CTRL simulation in winter and summer over 2010–2018 with extremums and mean values of differences listed upon.

(Figures 12f and 12l) largely depend on the deviations of ET simulation (Figure 10) which are merely evident in humid and semi humid areas. In winter, relatively obvious negative (positive) deviations appear around the Hengduan Mountains in southeast Tibet, the southern hillside areas and the Taiwan (the Qinling Mountain and the Yunnan-Guizhou Plateau) (Figure 12f). In summer, negative differences of LH near the Hengduan Mountains are much more significant (Figure 12l).

As to the simulation of hydrological process, the spatial distributions of snow cover and snow depth modeled by the CTRL experiment are conformable. The snow coverage during winter reach more than 80% in the north of the Tianshan Mountains, northern edge of the TP and northeast China (Figure 13a), where the maximum snow depth appears (Figure 13b). The snow over most China melts rapidly in spring and disappears in summer (except for TP where the snow maintains on the northern slope of the plateau and near the Karakoram Mountains) (Figures 14i and 14j). Distributions of differences in the simulated snow depth and snow cover are consistent with that of modeled LST differences (Figure 9), suggesting that the simulation of snow is significantly affected by the simulation of LST. In winter (Figures 14e and 14f), adopting the 3D STSRE scheme reduces the LST overestimated by the CTRL experiment in most mountainous areas due to the attenuated surface NR, thus increases the snow cover (up to 36.7%) and the snow depth (up to 92.9 mm). The simulated snow decreases only at a few sunlit slopes such as southern foothills of the Kunlun Mountains and the Tianshan Mountains thanks to the increases of SDSR, so the regional mean snow depth increases by 1.07 mm in the SEXP experiment compared to the CTRL experiment. In summer (Figures 13m and 13n), the increases of modeled snow cover (up to 6.04%) and snow depth (up to 86.1 mm) in the SEXP experiment relative to the CTRL experiment only appear over rugged terrains, for example, the Kunlun Mountains and Hengduan Mountains severely influenced by the topographical shading (Figure 1b).

The spatial patterns of surface runoff and soil moisture (SSM, in soil layers at the depth of 0–10 cm) simulated by the CTRL experiment basically decrease from southeast to northwest during winter and summer. The differences in modeled surface runoff between SEXP and CTRL experiments show distinct responses to the areas with different snow cover conditions in winter (Figure 13g). For example, compared with the CTRL experiment, the

10.1029/2023JD039775

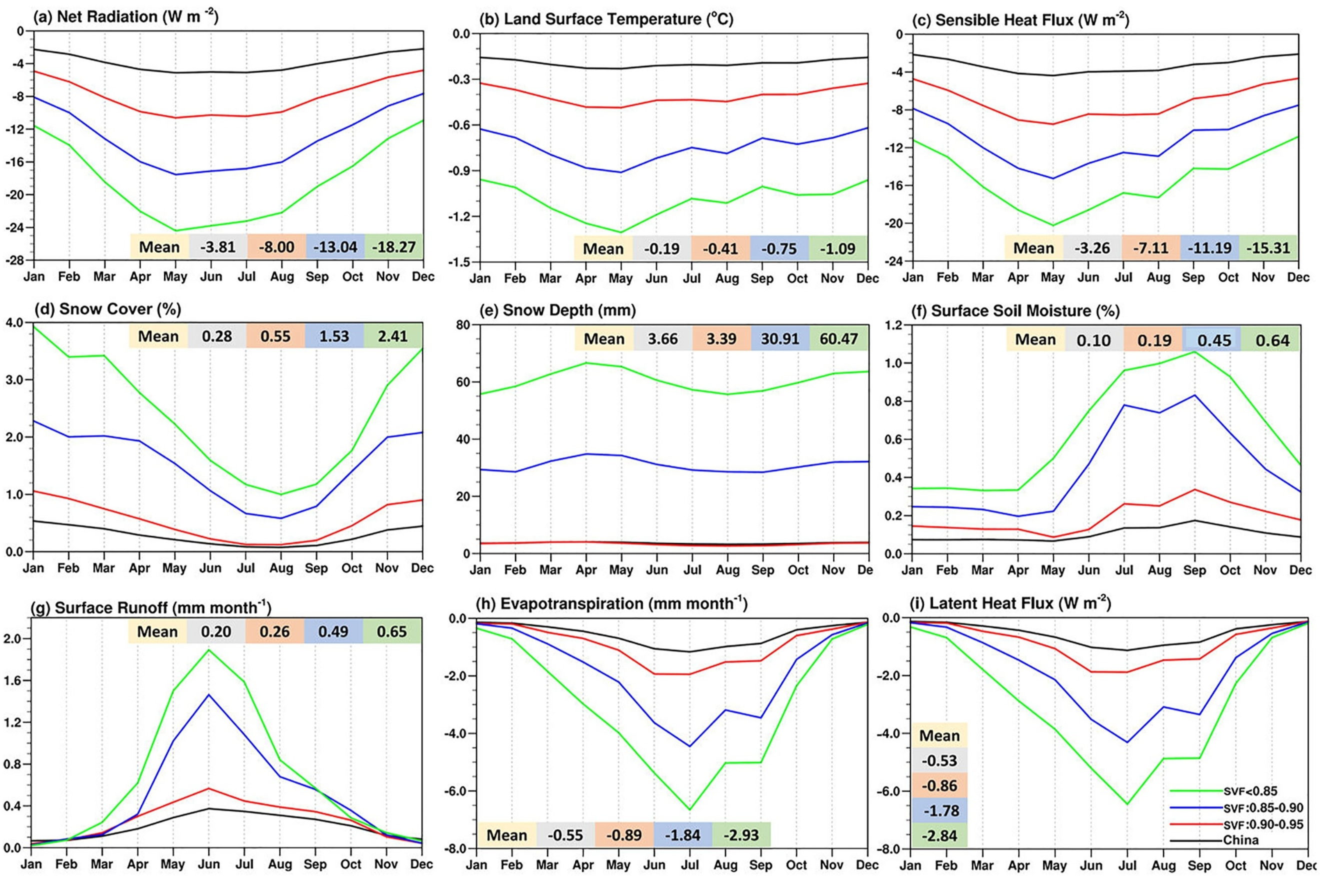

Figure 14. The monthly variation of multiyear mean differences between the SEXP experiment and CTRL experiment for NR (a), LST (b), SH (c), snow cover (d), snow depth (e), SSM (f), surface runoff (g), ET (h), and LH (i) regionally averaged over the regions with different SVF and the entire China during 2010–2018. The annual mean differences for different regions listed upon are shaded with corresponding colors.

surface runoff modeled by the SEXP experiment decreases (up to 11.46 mm month^{-1}) in snow-capped alpine areas (i.e., the northwest of the TP, the Tianshan Mountains, the Changbai Mountains) since the snow melt water supply reduces in spring owing to the increase of simulated snow cover and depth (Figures 13e and 13f), the inhibited ET (Figure 10) caused by the reduced SDSR and corresponding reduction of LST induced by the STSRE, so the regional mean deviation is only 0.073 mm month^{-1}.

In summer, the positive deviations of SSM in the SEXP experiment compared to the CTRL experiment (Figure 13o) in northern TP, the Hengduan Mountains, the Qinling Mountains and Taiwan Mountains are very obvious because of the water supplement of alpine snow melting in spring with the maximum of 119.03 mm month^{-1} and the regional mean difference of 0.344 mm month^{-1} (about 4.72 times of that in winter). The spatial pattern of modeled SSM differences between SEXP and CTRL (Figures 13h and 13p) is jointly controlled by the simulation differences of surface runoff and ET (Figure 10). Positive changes of SSM simulated by the SEXP experiment relative to the CTRL experiment in winter (Figure 13h) is accordingly large around the Qilian Mountains, Qinling Mountains and Hengduan Mountains due to the increases of the SSM in summer (Figure 13l), the intensity of modeled SSM differences between the SEXP and CTRL experiments (Figure 13p) is significantly greater than that in winter with the regional mean up to 0.16% (about 1.4 times of that in winter).

From Figures 12 and 13, the magnitude of differences in the simulation of surface heat fluxes and hydrological process induced by the 3D STSRE is closely related to the complexity of surrounding terrains represented by the SVF (Figure 1b). To quantitatively demonstrate the impacts of terrain complexity on simulation differences and their seasonal variations, we again partition the whole research area into several regions same as Figure 11, and calculate the monthly variation of regionally averaged deviations and relative differences in the simulated surface

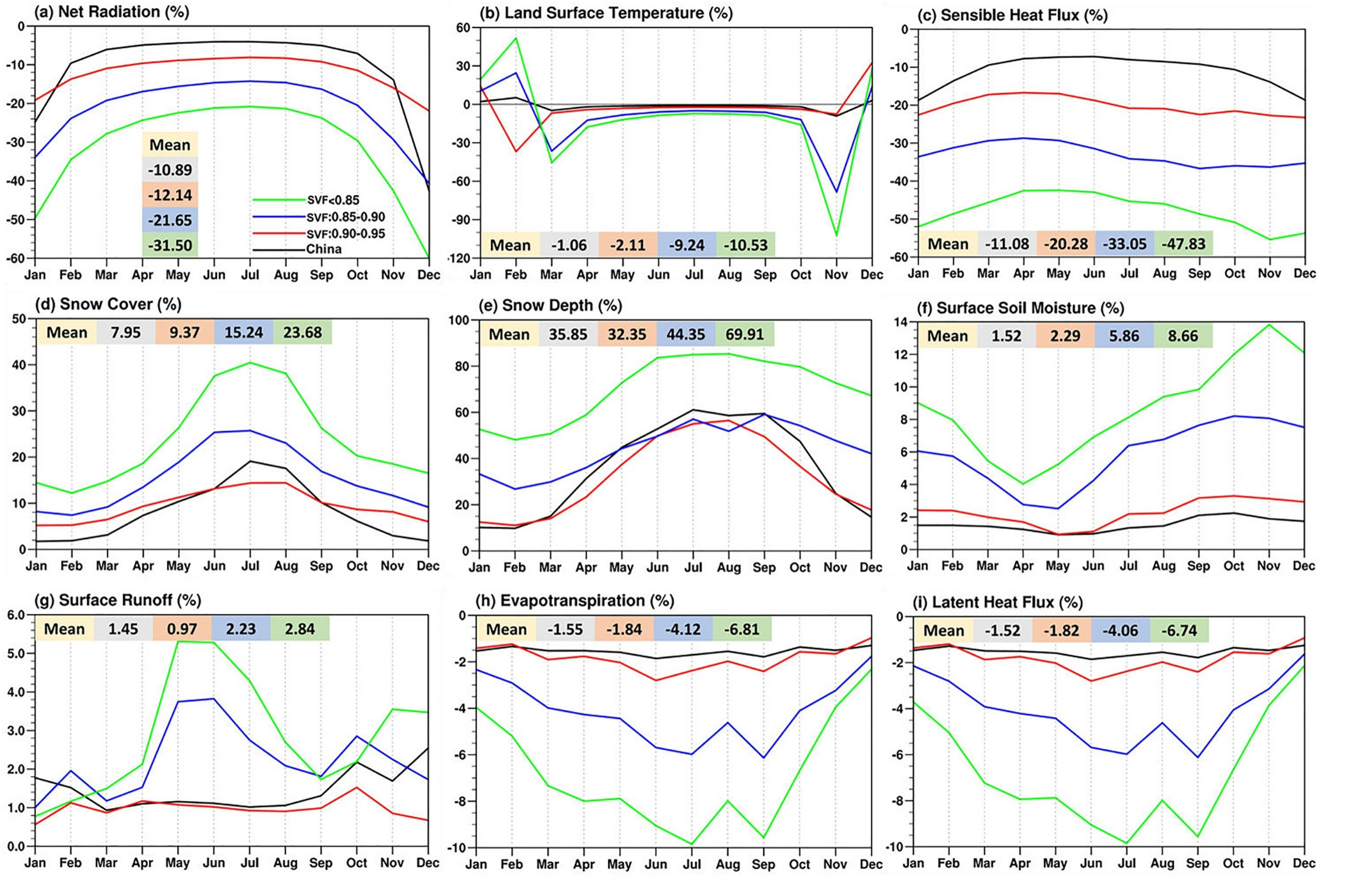

Figure 15. The monthly variation of multiyear mean relative differences between the SEXP and CTRL ((SEXP − CTRL)/CTRL × 100%) for NR (a), LST (b), SH (c), snow cover (d), snow depth (e), SSM (f), surface runoff (g), ET (h), and LH (i) regionally averaged over the regions with different SVF and the entire China during 2010–2018. The annual mean relative differences for different regions listed upon are shaded with corresponding colors.

NR, LST, SH, snow cover, snow depth, SSM, surface runoff, ET and LH for the regions with different SVF (Figures 14 and 15).

Overall, the smaller SVF indicating more complicated surrounding terrain well corresponds to the greater simulation differences and the more significant relative differences of each parameter, and vice versa (Figures 14 and 15). For the surface NR, the negative differences between the SEXP and CTRL experiments become greater when shading effects of surrounding mountains get stronger, so the annual mean differences over the regions with SVF < 0.85 is the largest among the 3 classifications of SVF (Figure 14a) with a relative change of −31.5% (Figure 15a). Among all classifications, differences in winter are relatively smaller compared to the other seasons. The minimum negative difference occurs in March, reaching −24.40 W m^{-2}. However, the relative differences in the modeled NR between SEXP and CTRL (Figure 15a) are more significant in winter (even reaching 59.9% in December) due to the low solar elevation angle and the corresponding strong topographical shading effect.

The simulation of LST is mainly controlled by the radiation heating, therefore seasonal variations of modeled LST discrepancies between the two experiments (Figure 14b) are very analogous to those of the modeled surface NR differences (Figure 14a). Negative deviations are obvious throughout the year, especially in spring with a minimum of −1.31°C over the regions with SVF < 0.85 in May. The deviations of simulated SH (Figure 14c) are primarily controlled by those of LST simulation and thus exhibits consistent temporal pattern with the modeled LST deviations, showing a maximum in spring with a mean value of −18.33 W m^{-2} over the regions with the SVF < 0.85. Meanwhile, relative differences in the LST and SH simulations are comparable with those of the surface NR simulations (Figures 15a–15c), which are more remarkable in autumn and winter due to relatively lower solar elevation angle.

The snow cover also increases correspondingly with the decrease of LST, so that the positive differences of modeled snow cover between the SEXP experiment and CTRL experiment are the largest (smallest) in winter (summer) among four seasons (Figure 14d). Significant negative deviations of the modeled LST in winter and spring could further retard the snow melting process over the snow-capped mountains in spring, bringing the positive deviations of simulated snow depth (Figure 14e) in the regions with the SVF < 0.85 (0.85 < SVF < 0.90) become the largest with a positive deviation of 66.63 mm (34.80 mm) in spring among four seasons. While the seasonal variations of simulated snow depth deviations over the regions with the SVF > 0.90 are much smaller. Moreover, the reduction of modeled LST in the SEXP experiment would also inhibit the land surface evapotranspiration process and further weaken the LH simulation. Therefore, for the regions with the SVF less than 0.90, differences in the simulated ET and LH (Figures 14h and 14i) increase rapidly when snow melt water supply increases in spring, reaching the maximum in July. Seasonal variations of relative differences in the ET and LH between the two experiments are roughly the same (Figures 15h and 15i) and both reach peak values in July.

In the soil hydrological simulations of the CoLM, the water seeping into the underground, namely the sum of soil water content and surface runoff, is expressed as the sum of snow melting and precipitation minus the ET. Therefore, differences in the simulated SSM and surface runoff are jointly dominated by the snow cover and ET. The flow size of surface runoff in the alpine snow covered areas with the SVF < 0.90 is mainly regulated by the snow melt water (Figures 10 and 13), thus the increase of snow cover simulation reduces the runoff simulation in winter and spring (Figure 14g). While in the areas without snow cover, the decrease of ET simulation plays a dominant role in supplementing the simulated surface runoff. As can be seen from the average values over the regions with different SVF and the whole China, the differences in surface runoff simulation between the two experiments maintain positive throughout the year mainly affected by the differences in ET simulation, with the annual mean differences ranging from 0.20 mm month^{-1} to 0.65 mm month^{-1}. Positive differences increase rapidly since March and peak in June (with the maximum of 1.89 mm month^{-1} in the areas of SVF < 0.85 and 1.46 mm month^{-1} in the areas of 0.85 < SVF < 0.90, respectively) because of snow melting supplement to the surface water cycle in spring.

Deviations of SSM simulation (Figure 14f) are cooperatively controlled by the differences in surface runoff and ET simulations, and show obvious positive values throughout the year due to the reduction of modeled ET, which can reach 0.99% annually over the regions with the SVF < 0.85. Besides, differences in the modeled runoff affect the intensity of differences in SSM simulation. For the regions with the SVF < 0.90, the rapid increase of modeled surface runoff differences alleviates the enlargement of deviations in SSM simulation during spring. When the modeled surface runoff differences rapidly decrease after June, positive deviations of SSM simulation continue to grow until autumn and reach the maximum in September. The seasonal variation of simulated surface runoff and SSM changes induced by the 3D STSRE can be clearly shown by the relative differences (Figures 15f and 15g). The relative differences in the modeled surface runoff simulation (Figure 15g) over the mountainous areas with SVF < 0.90 increase rapidly from March and drops quickly after reaching the annual peak in May or June.

Meanwhile, the relative differences in the SSM simulation (Figure 15f) increase steadily from March and become the most prominent in November due to the instant decline of modeled SSM concerned with the gradual frozen soil during autumn and winter. The increase of SSM will also in turn strengthen the ET (Lawrence & Slingo, 2005; Xu & Singh, 2005) especially in the arid and semi-arid areas, and further leads to decrements in the intensity of negative deviations in ET simulation, forming a negative feedback process for the intensity of simulated differences between the SSM and ET. Therefore, the relative differences of the modeled ET (Figure 15h) are the weakest from October to the following February, when the relative differences in modeled SSM rise up to the maximum (Figure 15f).

Overall, for the areas strongly shaded by surrounding terrains such as the north slope and southeastern part of TP and the southeastern hillside areas, adopting the 3D STSRE scheme can well reduce the LST warm biases in the CoLM using the plane-parallel radiative scheme due to the decrease of simulated surface NR. On the one hand, the reduced LST directly controls the decrease in SH and upward longwave radiation. On the other hand, the depressed LST promotes the accumulation of snowfall to diminish the surface runoff and SSM through the reduction of snow melt water, and inhibits the ET simulation to depress the LH flux, resulting in the increases of surface runoff and SSM at the same time. On the contrary, for the areas with sunlit slope such as the southern hillside of Tianshan Mountains, much more absorbed SDSR leads to much higher LST and thereafter increment in the modeled SH and LH due to the 3D STSRE.

10.1029/2023JD039775

4. Discussions

In the SEXP experiment, the direction of the SDSR flux over mountainous areas is perpendicular to the inclined surface, while that in the CTRL experiment and GLASS data is perpendicular to the horizontal plane. As many previous studies (Gu et al., 2024; Huang et al., 2022; Ma et al., 2024; Xian et al., 2023; Yan et al., 2016, 2020), we just adopt the area weighted average method (Equations 1–8) to aggregate the SDSR at sub-grids to model grids in this study, this may lead to the directions of SDSR fluxes produced by the SEXP experiment in mountainous areas are non-vertical. To reveal the impact of this processing on the results to what extent, we carried out an additional experiment named SEXP1 which is the same as SEXP experiment, except that the SEXP1 experiment adopts the method of the vertical projection of SDSR. Results show that the vertical projection process adopted in the SEXP1 experiment slightly affects the terrain-corrected SDSR fluxes compared to the SEXP experiment (Figures S1 to S3 in Supporting Information S1), the relative differences of SDSR fluxes produced by the SEXP1 experiment relative to the SEXP experiment at nearly 90% of the rugged grid points which have the SVF < 0.99 are within $\pm 1\%$. Even in the most rugged regions with the SVF < 0.85, the absolute relative differences of SDSR fluxes between SEXP1 and SEXP are less than 3% all year round. The above analysis confirms that the projection of SDSR onto the vertical direction barely affects the main conclusions obtained by this study adopting the area weighted methods. Despite that the main conclusions in this study are robust, we should project the SDSR flux onto the vertical direction in the future studies.

In addition, limitations of the validation data sets still exist due to relatively poor performances of remote sensing data sets over complex terrains, though they show reasonable evaluation results with observations in mountainous areas mentioned in data introduction section. For example, Liu et al. (2023) found that although the daily GLASS SDSR show good consistency with ground measurements of 48 sites in China, it also exhibits obvious biases over the TP. As we mentioned in Section 2.3, the GLASS product incorporates the surface elevation correction, while the impacts of topography is not fully considered. Hence, we choose the H8 SDSR data set (Letu et al., 2022) that considers the terrain effect in the TP region as the additional benchmarking data set to study the influence of the 3D STSRE scheme on the performance of CoLM in simulating the SDSR.

Furthermore, we carried out three additional experiments over the TP region to validate the model performance in simulating LST, snow cover and ET (Figures 16c–16k): the experiment driven by the CMFD without (with) the 3D STSRE scheme is called CMFD (STSRE), and the experiment driven by the CMFD data with CMFD SDSR replaced by the H8 SDSR is named as H8. As the H8 data only covers 3-years period from 2016 to 2018, all experiments were performed 12 years cyclically driven by the forcing data from 1 January 2016 to 31 December 2018, and the last 3 years were extracted for subsequent analysis.

From Figure 16a, the CMFD SDSR data shows obvious positive deviation over the TP relative to the H8 SDSR data. After the correction of the 3D STSRE scheme, the bias of CMFD SDSR in the mountainous areas can be significantly reduced (Figure 16b) with the Ts (RMSE) in the STSRE experiment increased from 0.892 in the CMFD to 0.933 (decreased from 11.64 W m^{-2} in the CMFD to 10.73 W m^{-2}). This result indicates that adopting the 3D STSRE scheme can indeed improve the SDSR over complex terrains.

From quantitative analysis results (Figures 16c–16k), the STSRE experiment shows superior performance than the CMFD experiment with clearly smaller RMSE (higher Ts) concerning all three variables. Moreover, the modeling performance of the STSRE experiment is just slightly inferior to that of the H8 experiment, suggesting that adopting the 3D STSRE scheme in the CoLM can obtain comparable performance with the simulation directly driven by the SDSR with the terrain effect. The main problems hindering the application of SDSR data sets including STSRE are applicable range not wide enough and difficult to acquire in real-time, which could be well solved by implementing the 3D STSRE scheme into LSMs to make up the modeling deficiencies of the plane-parallel SDSR over the rugged terrains.When employed in the coupled climate models, the 3D STSRE scheme may help improve the simulation of radiative transfer and land-atmosphere interaction over complex terrains (Gu et al., 2022). Besides, as the fact that the insufficient and discontinuous meteorological stations cannot meet the needs of validations for model performances in complex terrains, we still choose the GLASS data sets for model evaluations owing to their long-temporal and spatial continuity over mountainous areas.

10.1029/2023JD039775

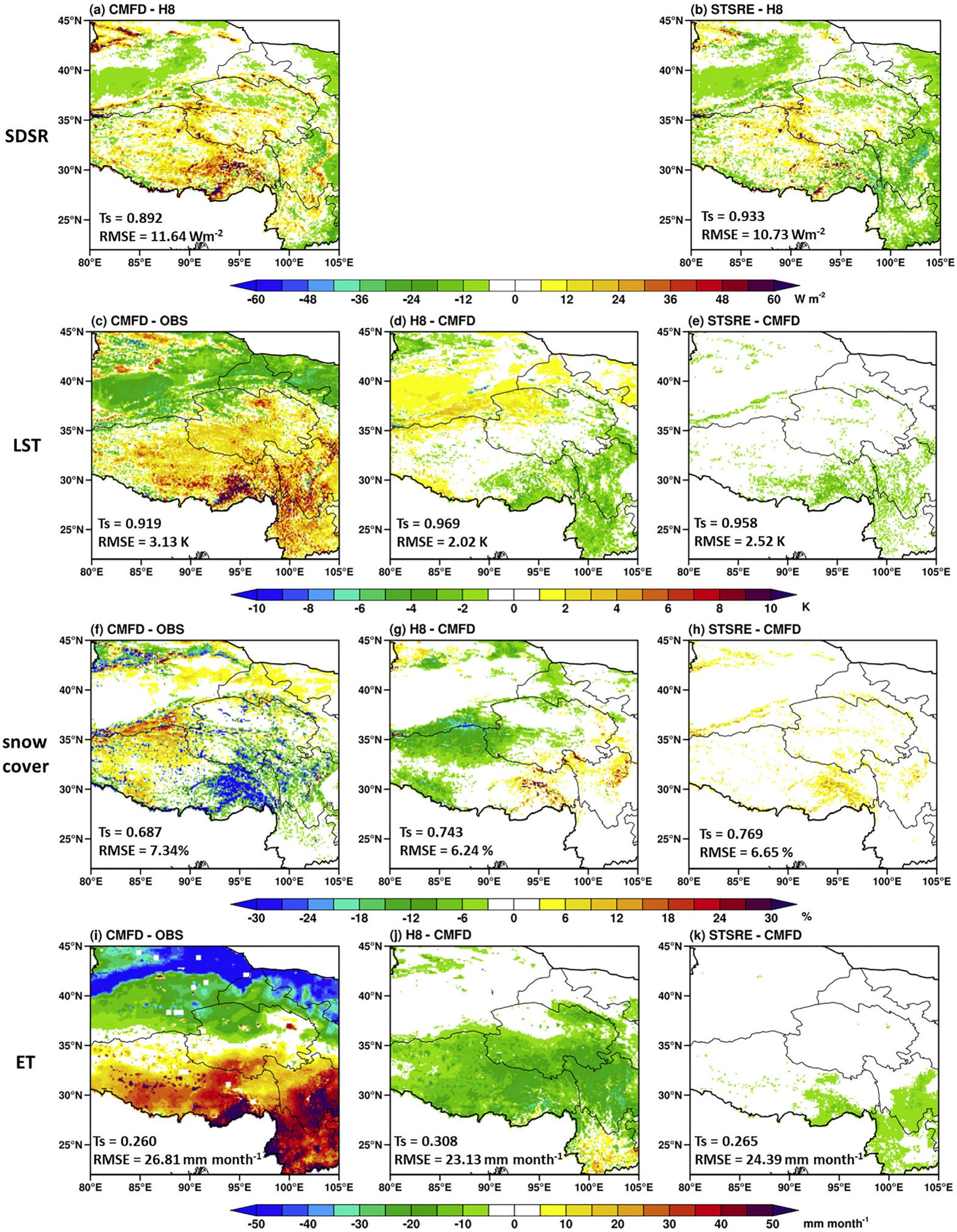

Figure 16.

5. Conclusions

In this paper, we focus on elaborately describe the surface solar radiation process considering the sub-grid terrain effect to reduce the errors in the SDSR forcing data without the terrain effect, and discuss the impacts of the 3D STSRE scheme on model performance in simulating the surface heat budget and hydrological processes over rugged terrains in China. The main findings are concluded as follows:

1. The CoLM model coupled with the 3D STSRE scheme well corrects the overestimation of SDSR in the original plane-parallel radiative transfer scheme, leading to the remarkable decreases of RMSE and prominent increases of Taylor score in all seasons. And the improvements of the SDSR increase with the terrain complexity increasing.
2. Validations against observations show that considering the 3D STSRE distinctly improves the simulations of key land surface parameters in the CoLM over mountainous areas with different climate conditions, and the more rugged the terrain is, the more important influences the 3D STSRE scheme exerts on the improvements of key variable simulations.
3. Further analysis reveals that over mountainous areas, the 3D STSRE scheme firstly influences the simulation of LST by changing the NR. Then the changed LST directly affects the SH flux through altering the temperature gradient between land surface and atmosphere. On the other hand, it exerts influences on the ET and snow accumulation (melting) processes, that jointly control the simulation of runoff and SSM, and finally modifies the LH flux simulation.

In summary, we have addressed the quantitative impacts of sub-grid landforms on the land thermal and hydrological processes over complex terrain areas in China, providing insight into the possible causes related to the influence of 3D STSRE on modeling the land surface processes. Although simulations of SDSR, LST and snow cover are prominently improved with the consideration of the 3D STSRE, the improvements of ET simulation over the areas covered with forest land type is relatively small due to the large systematic error in the original CoLM, which may be related to the original parameter settings of the model. On one hand, the leaf area index (LAI) data set applied in the CoLM is directly subtracted from the MODIS LAI data set, without considering the dynamic impact of terrain heterogeneity on vegetation characteristics (Hwang et al., 2011; Kayiranga et al., 2017; Wood et al., 2011) by affecting the local microclimate of mountainous areas (such as precipitation and solar fluxes absorbed by the canopy).

It is necessary to profoundly study the 3D STSRE on the simulation of dynamic vegetation canopy (i.e., the vegetation coverage type and LAI), so as to further improve the characterization of the transpiration process of tree leaves and the evaporation process of canopy precipitation interception in densely vegetated mountains. On the other hand, the sub-grid topography could not only exert influences on the local water cycle of slope surfaces through thermal heterogeneity, but also directly controls important dynamic processes such as subsurface flows and lateral surface flows, that may play a vital part in modeling soil water profiles and ET at mountainous watershed (Chang et al., 2018; Ji et al., 2017). Combining the 3D STSRE scheme with the sub-grid runoff model, the hydrological process on slope surface is expected to be elaborately described and then to promote the potential of ET and soil moisture profile simulations.

Additionally, simulations of other fluxes that help balance the surface net shortwave radiation flux, like longwave radiation flux, sensible heat flux and latent heat flux, are also affected by various sub-grid scale topographic features. Thus, our team (Gu et al., 2024) have proposed a 3D sub-grid terrain longwave radiative effect parameterization scheme to reduce the biases of plane-parallel scheme over the TP. However, modeling sub-grid-scale interactions between topography and the sensible and latent heat fluxes is still a great challenge, since the variables including the surface air temperature, humidity, wind speed and air pressure for the calculations of sensible and latent heat fluxes are uniform on all sub-grids within a given model grid in present CoLM, which is not conformed with real cases. How to disaggregate the relevant variables from model grid to its sub-grids based

Figure 16. The spatial distribution of differences in the annual mean surface downward solar radiation (a) between the CMFD and H8, and (b) between the sub-grid terrain solar radiative effect (STSRE) and H8 over 2016–2018. The root mean squared error (RMSE) and Ts values in CMFD and STSRE experiments relative to the H8 experiment are listed at the corners. The annual mean differences of land surface temperature (c–e), snow cover (f–g) and ET (i–k) simulations between the CMFD and OBS (left), between the H8 and CMFD (middle), and between the STSRE and CMFD (right) over 2016–2018. The RMSE and Ts values for each variable produced by the CMFD, H8, STSRE experiments relative to OBS are listed at the bottom.

on different sub-grid terrain conditions needs further study to describe sub-grid-scale topographic impacts on sensible and latent heat flux. It is indicated that although the 3D STSRE is more significant at finer horizontal resolutions, its subsequent impacts on simulating the surface heat fluxes, LST and snow cover could still be remarkable at the horizontal resolution as coarse as 2° in the TP (Hao et al., 2021; Nian, 2020). Nevertheless, these researches only focus on the differences of simulating parameters introduced by the 3D STSRE scheme and neglect validations against observations to analyze the sensitivity of the 3D STSRE on the model capabilities in simulating key land surface variables to model resolution. Hence, a study is underway to thoroughly investigate the sensitivity of the impact of 3D STSRE on simulating the key surface parameters such as LST, snow cover and ET over mountainous areas to model resolution.

Moreover, with the resolution of numerical models increasing, the importance of realistically parameterizing the sub-grid scale orographic dynamic process is also highlighted that the implement of orographic drag effects containing the turbulent orographic form drag and the gravity wave drag can substantially improve the capability in modeling precipitation and wind over hilly terrains such as the TP and the south China (Xue et al., 2021; Zhong & Chen, 2015; Zhou et al., 2019). Besides, supplementing the sub-grid scale thermal feedback induced by the 3D STSRE scheme in climate models could also advance the simulation of precipitation and air temperature over the TP (G. Y. Chen et al., 2019; Gu et al., 2020, 2022). However, the thermal and dynamic impacts of sub-grid topography are often separately considered in numerical models so that researches on their combined influences and underlying mechanisms are rarely reported. Therefore, the subsequent research needs to build a scheme that coordinates the thermal forcing and dynamic drag effects of the sub-grid landform to comprehensively consider the dynamic and thermal effects of sub-grid topography in climate models.

Data Availability Statement

Data - The China Meteorological Forcing Dataset and the monthly China land surface temperature product are available at http://poles.tpdc.ac.cn. The Shuttle Radar Topography Mission (SRTM) 90 m Digital Elevation Database v4.1 used in this study is available at https://developers.google.com/earth-engine/datasets/catalog/CGIAR_SRTM90_V4. The Global Land Surface Satellite (GLASS) DSSR product can be downloaded from http://www.geodata.cn. The third version of the Global Land Evaporation Amsterdam Model (GLEAM v3) ET product is provided from https://www.gleam.eu. The monthly snow cover data can be download from https://search.earthdata.nasa.gov/search. Software - The source codes of the CoLM Version 2014 are available at http://globalchange.bnu.edu.cn/research/models.

Acknowledgments

This work is founded by the National Natural Science Foundation of China under Grants 42375157, CAS "Light of West China" Program (E129030101), Open Research Fund Program of Plateau Atmosphere and Environment Key Laboratory of Sichuan Province (PAEKL-2023-K01), the Jiangsu University "Blue Project" outstanding young teachers training object, and the Jiangsu Collaborative Innovation Center for Climate Change. We appreciate the High performance Computing Center of Nanjing University and the National Key Scientific and Technological Infrastructure project "Earth System Numerical Simulation Facility" (EarthLab) for providing us the computing resource. We sincerely thank the National Tibetan Plateau Data Center, National Earth System Science Data Center, National Science and Technology Infrastructure of China, CIAT, GLEAM and NSIDC for allowing us to use these data.

References

Aguilar, C., Herrero, J., & Polo, M. J. (2010). Topographic effects on solar radiation distribution in mountainous watersheds and their influence on reference evapotranspiration estimates at watershed scale. *Hydrology and Earth System Sciences*, *14*(12), 2479–2494. https://doi.org/10.5194/hess-14-2479-2010

Akash, K., & Petra, H. (2022). The third version of the Global Land Evaporation Amsterdam Model (GLEAM v3) ET product [Dataset]. https://www.gleam.eu

Arnold, N. S., Rees, W. G., Hodson, A. J., & Kohler, J. (2006). Topographic controls on the surface energy balance of a high Arctic valley glacier. *Journal of Geophysical Research*, *111*(F2). https://doi.org/10.1029/2005jf000426

Arthur, R. S., Lundquist, K. A., Mirocha, J. D., & Chow, F. K. (2018). Topographic effects on radiation in the WRF model with the immersed boundary method: Implementation, validation, and application to complex terrain. *Monthly Weather Review*, *146*(10), 3277–3292. https://doi.org/10.1175/mwr-d-18-0108.1

Barry, R. G. (1992). *Mountain weather and climate* (3rd ed.). Cambridge University Press.

Chang, L. L., Dwivedi, R., Knowles, J. F., Fang, Y. H., Niu, G. Y., Pelletier, J. D., et al. (2018). Why do large-scale land surface models produce a low ratio of transpiration to evapotranspiration? *Journal of Geophysical Research-Atmospheres*, *123*(17), 9109–9130. https://doi.org/10.1029/2018jd029159

Chen, G. Y., Wei, Z. G., Dong, W. J., Zhu, X., Chen, C., Liu, Y. J., & Zhang, Z. J. (2019). Effects of improvement of land surface subgrid topographic parameterization on regional temperature and precipitation simulation in Western China. *Chinese Journal of Atmospheric Sciences*, *43*(4), 846–860. https://doi.org/10.3878/j.issn.1006-9895.1807.18156

Chen, L., Yan, G., Wang, T., Ren, H., Calbo, J., Zhao, J., & McKenzie, R. (2012). Estimation of surface shortwave radiation components under all sky conditions: Modeling and sensitivity analysis. *Remote Sensing of Environment*, *123*, 457–469. https://doi.org/10.1016/j.rse.2012.04.006

Chen, Y., Hall, A., & Liou, K. N. (2006). Application of three-dimensional solar radiative transfer to mountains. *Journal of Geophysical Research*, *111*(D21). https://doi.org/10.1029/2006jd007163

Chen, Y., & Liou, K. N. (2006). A Monte Carlo method for 3D thermal infrared radiative transfer. *Journal of Quantitative Spectroscopy & Radiative Transfer*, *101*(1), 166–178. https://doi.org/10.1016/j.jqsrt.2005.10.002

Chen, Y., Liou, K. N., & Gu, Y. (2005). An efficient diffusion approximation for 3D radiative transfer parameterization: Application to cloudy atmospheres. *Journal of Quantitative Spectroscopy & Radiative Transfer*, *92*(2), 189–200. https://doi.org/10.1016/j.jqsrt.2004.07.029

Dai, Y. (2014). The Common Land Model (CoLM) version 2014 (no CaMa-flood model) [Software]. http://globalchange.bnu.edu.cn/research/models

Dai, Y., Zhang, S., Yuan, H., & Wei, N. (2019). Modeling variably saturated flow in stratified soils with explicit tracking of wetting front and water table locations. *Water Resources Research*, *55*(10), 7939–7963. https://doi.org/10.1029/2019WR025368

Dai, Y. J., Zeng, X. B., Dickinson, R. E., Baker, I., Bonan, G. B., Bosilovich, M. G., et al. (2003). The Common Land Model. *Bulletin of the American Meteorological Society*, *84*(8), 1013–1023. https://doi.org/10.1175/Bams-84-8-1013

Dirksen, M., Ronda, R. J., Theeuwes, N. E., & Pagani, G. A. (2019). C Sky view factor calculations and its application in urban heat island studies. *Urban Climate*, *30*, 100498. https://doi.org/10.1016/j.uclim.2019.100498

Dozier, J., & Frew, J. (1990). Rapid calculation of terrain parameters for radiation modeling from digital elevation data. *IEEE Transactions on Geoscience and Remote Sensing*, *28*(5), 963–969. https://doi.org/10.1109/36.58986

Dubayah, R., & Rich, P. M. (1995). Topographic solar-radiation models for GIS. *International Journal of Geographical Information Systems*, *9*(4), 405–419. https://doi.org/10.1080/02693799508902046

Evans, K. F. (1998). The spherical harmonics discrete ordinate method for three-dimensional atmospheric radiative transfer. *Journal of the Atmospheric Sciences*, *55*(3), 429–446. https://doi.org/10.1175/1520-0469(1998)055<0429:Tshdom>2.0.Co;2

Fan, X. H., Gu, Y., Liou, K. N., Lee, W. L., Zhao, B., Chen, H. B., & Lu, D. R. (2019). Modeling study of the impact of complex terrain on the surface energy and hydrology over the Tibetan Plateau. *Climate Dynamics*, *53*(11), 6919–6932. https://doi.org/10.1007/s00382-019-04966-z

Fu, B. P. (1983). *Mountain climate (in Chinese)*. Science Press.

Gu, C., Huang, A., Li, X., Yang, B., & Wu, Y. (2024). Construction of a clear-sky three dimensional sub-grid terrain long-wave radiative effect parameterization scheme under isotropic assumption. *Journal of Geophysical Research: Atmospheres*, *129*(4), e2023JD039383. https://doi.org/10.1029/2023JD039383

Gu, C., Huang, A., Wu, Y., Yang, B., Mu, X., Zhang, X., & Cai, S. (2020). Effects of subgrid terrain radiative forcing on the ability of RegCM4.1 in the simulation of summer precipitation over China. *Journal of Geophysical Research- Atmospheres*, *125*(12). https://doi.org/10.1029/2019jd032215

Gu, C., Huang, A., Zhang, Y., Yang, B., Cai, S., Xu, X., et al. (2022). The wet bias of RegCM4 over Tibet Plateau in summer reduced by adopting the 3D sub-grid terrain solar radiative effect parameterization scheme. *Journal of Geophysical Research: Atmospheres*, *127*(21). https://doi.org/10.1029/2022JD037434

Gu, Y., Liou, K. N., Lee, W. L., & Leung, L. R. (2012). Simulating 3-D radiative transfer effects over the Sierra Nevada Mountains using WRF. *Atmospheric Chemistry and Physics*, *12*(20), 9965–9976. https://doi.org/10.5194/acp-12-9965-2012

Hall, D. K., & Riggs, G. A. (2021a). MODIS/Terra snow cover monthly L3 global 0.05Deg CMG, version 61 [Dataset]. *NASA National Snow and Ice Data Center Distributed Active Archive Center*. https://doi.org/10.5067/MODIS/MOD10CM.061

Hall, D. K., & Riggs, G. A. (2021b). MODIS/Aqua snow cover monthly L3 global 0.05Deg CMG, version 61 [Dataset]. *NASA National Snow and Ice Data Center Distributed Active Archive Center*. https://doi.org/10.5067/MODIS/MYD10CM.061

Hao, D. L., Bisht, G., Gu, Y., Lee, W. L., Liou, K. N., & Leung, L. R. (2021). A parameterization of sub-grid topographical effects on solar radiation in the E3SM Land Model (version 1.0): Implementation and evaluation over the Tibetan Plateau. *Geoscientific Model Development*, *14*(10), 6273–6289. https://doi.org/10.5194/gmd-14-6273-2021

Hauge, G., & Hole, L. R. (2003). Implementation of slope irradiance in Mesoscale Model version 5 and its effect on temperature and wind fields during the breakup of a temperature inversion. *Journal of Geophysical Research*, *108*(D2). https://doi.org/10.1029/2002jd002575

He, J., Yang, K., Tang, W., Lu, H., Qin, J., Chen, Y. Y., & Li, X. (2020). The first high-resolution meteorological forcing dataset for land process studies over China. *Scientific Data*, *7*(1), 25. https://doi.org/10.1038/s41597-020-0369-y

He, J. L., Zhao, W., Li, A. N., Wen, F. P., & Yu, D. J. (2019). The impact of the terrain effect on land surface temperature variation based on Landsat-8 observations in mountainous areas. *International Journal of Remote Sensing*, *40*(5–6), 1808–1827. https://doi.org/10.1080/01431161.2018.1466082

He, S. W., Smirnova, T. G., & Benjamin, S. G. (2019). A scale-aware parameterization for estimating subgrid variability of downward solar radiation using high-resolution digital elevation model data. *Journal of Geophysical Research-Atmospheres*, *124*(24), 13680–13692. https://doi.org/10.1029/2019jd031563

Helbig, N., Loewe, H., & Lehning, M. (2009). Radiosity approach for the shortwave surface radiation balance in complex terrain. *Journal of the Atmospheric Sciences*, *66*(9), 2900–2912. https://doi.org/10.1175/2009jas2940.1

Hock, R., & Holmgren, B. (2005). A distributed surface energy-balance model for complex topography and its application to Storglaciären, Sweden. *Journal of Glaciology*, *51*(172), 25–36. https://doi.org/10.3189/172756505781829566

Hu, Y., Bai, L., Wang, H., & Mi, X. (2013). Validation for downward shortwave radiation of GLASS product by the coordinated enhanced observation (in Chinese). *Advances in Meteorological Science and Technology*(5), 7. https://doi.org/10.3969/j.issn.2095-1973.2013.05.002

Huang, A., Gu, C., Zhang, Y., Li, W., Zhang, J., Wu, Y., et al. (2022). Development of a clear-sky 3D sub-grid terrain solar radiative effect parameterization scheme based on the mountain radiation theory. *Journal of Geophysical Research-Atmospheres*, *127*(13). https://doi.org/10.1029/2022jd036449

Huang, A., Zhao, Y., Zhou, Y., Yang, B., Zhang, L., Dong, X., et al. (2016). Evaluation of multisatellite precipitation products by use of ground-based data over China. *Journal of Geophysical Research-Atmospheres*, *121*(18), 10654–10675. https://doi.org/10.1002/2016jd025456

Hwang, T., Song, C. H., Vose, J. M., & Band, L. E. (2011). Topography-mediated controls on local vegetation phenology estimated from MODIS vegetation index. *Landscape Ecology*, *26*(4), 541–556. https://doi.org/10.1007/s10980-011-9580-8

Jarvis, A., Reuter, H. I., Nelson, A., & Guevara, E. (2008). The Shuttle Radar Topography Mission (SRTM) 90 m digital elevation Database v4.1 [Dataset]. *International Centre for Tropical Agriculture (CIAT)*. https://developers.google.com/earth-engine/datasets/catalog/CGIAR_SRTM90_V4

Ji, P., Yuan, X., & Liang, X. Z. (2017). Do lateral flows matter for the hyperresolution land surface modeling? *Journal of Geophysical Research-Atmospheres*, *122*(22), 12077–12092. https://doi.org/10.1002/2017jd027366

Kan, M., Huang, A., Zhao, Y., Zhou, Y., Yang, B., & Wu, H. (2015). Evaluation of the summer precipitation over China simulated by BCC_CSM model with different horizontal resolutions during the recent half century. *Journal of Geophysical Research: Atmospheres*, *120*(10), 4657–4670. https://doi.org/10.1002/2015JD023131

Kayiranga, A., Ndayisaba, F., Nahayo, L., Karamage, F., Nsengiyumva, J. B., Mupenzi, C., & Nyesheja, E. M. (2017). Analysis of climate and topography impacts on the spatial distribution of vegetation in the Virunga Volcanoes Massif of East-Central Africa. *Geosciences*, *7*(1), 17. https://doi.org/10.3390/geosciences7010017

Kim, H. Y., & Liang, S. L. (2010). Development of a hybrid method for estimating land surface shortwave net radiation from MODIS data. *Remote Sensing of Environment*, *114*(11), 2393–2402. https://doi.org/10.1016/j.rse.2010.05.012

Lawrence, D. M., & Slingo, J. M. (2005). Weak land-atmosphere coupling strength in HadAM3: The role of soil moisture variability. *Journal of Hydrometeorology*, *6*(5), 670–680. https://doi.org/10.1175/Jhm445.1

Lee, W. L., Liou, K. N., & Wang, C. C. (2013). Impact of 3-D topography on surface radiation budget over the Tibetan Plateau. *Theoretical and Applied Climatology*, *113*(1–2), 95–103. https://doi.org/10.1007/s00704-012-0767-y

Lee, W. L., Liou, K. N., Wang, C. C., Gu, Y., Hsu, H. H., & Li, J. L. F. (2019). Impact of 3-D radiation-topography interactions on surface temperature and energy budget over the Tibetan Plateau in Winter. *Journal of Geophysical Research-Atmospheres*, *124*(3), 1537–1549. https://doi.org/10.1029/2018jd029592

Letu, H., Nakajima, T. Y., Wang, T., Shang, H., Ma, R., Yang, K., et al. (2022). A new benchmark for surface radiation products over the East Asia–Pacific Region retrieved from the Himawari-8/AHI next-generation geostationary satellite. *Bulletin of the American Meteorological Society*, *103*(3), E873–E888. https://doi.org/10.1175/BAMS-D-20-0148.1

Li, C. W., Lu, H., Yang, K., Wright, J. S., Yu, L., Chen, Y. Y., et al. (2017). Evaluation of the Common Land Model (CoLM) from the perspective of water and energy budget simulation: Towards inclusion in CMIP6. *Atmosphere*, *8*(8), 141. https://doi.org/10.3390/atmos8080141

Li, J., & Luo, J. (2015). Estimation of solar radiation over rugged terrains based on clear sky condition. *Arid Land Geography*, *38*(1), 120–127.

Li, X., Cheng, G. D., Chen, X. Z., & Lu, L. (1999). Modification of solar radiation model over rugged terrain. *Chinese Science Bulletin*, *44*(15), 1345–1350. https://doi.org/10.1007/bf02885977

Li, X., Koike, T., & Cheng, G. (2002). Retrieval of snow reflectance from Landsat data in rugged terrain. *Annals of Glaciology*, *34*, 31–37. https://doi.org/10.3189/172756402781817635

Liou, K. N., Gu, Y., Leung, L. R., Lee, W. L., & Fovell, R. G. (2013). A WRF simulation of the impact of 3-D radiative transfer on surface hydrology over the Rocky Mountains and Sierra Nevada. *Atmospheric Chemistry and Physics*, *13*(23), 11709–11721. https://doi.org/10.5194/acp-13-11709-2013

Liou, K. N., Lee, W.-L., & Hall, A. (2007). Radiative transfer in mountains: Application to the Tibetan Plateau. *Geophysical Research Letters*, *34*(23), L23809. https://doi.org/10.1029/2007gl031762

Liu, T., Tao, H., Yichuan, M., & Xiaotong, Z. (2023). Evaluation and intercomparison of multiple satellite-derived and reanalysis downward shortwave radiation products in China. *International Journal of Digital Earth*, *16*(1), 1853–1884. https://doi.org/10.1080/17538947.2023.2212918

Lu, N., Qin, J., Yang, K., & Sun, J. L. (2011). A simple and efficient algorithm to estimate daily global solar radiation from geostationary satellite data. *Energy*, *36*(5), 3179–3188. https://doi.org/10.1016/j.energy.2011.03.007

Luo, S., Lue, S., & Zhang, Y. (2009). Development and validation of the frozen soil parameterization scheme in Common Land Model. *Cold Regions Science and Technology*, *55*(1), 130–140. https://doi.org/10.1016/j.coldregions.2008.07.009

Ma, Y., He, T., Aguilar, C., Pimentel, R., Liang, S., McVicar, T. R., et al. (2024). Evaluating topographic effects on kilometer-scale satellite downward shortwave radiation products: A case study in Mid-Latitude Mountains. *IEEE Transactions on Geoscience and Remote Sensing*, *62*, 1–16. https://doi.org/10.1109/TGRS.2024.3365865

Ma, Y. T., Pinker, R. T., Wonsick, M. M., Li, C., & Hinkelman, L. M. (2016). Shortwave radiative fluxes on slopes. *Journal of Applied Meteorology and Climatology*, *55*(7), 1513–1532. https://doi.org/10.1175/JAMC-D-15-0178.1

Martens, B., Miralles, D. G., Lievens, H., Fernandez-Prieto, D., & Verhoest, N. E. C. (2016). Improving terrestrial evaporation estimates over continental Australia through assimilation of SMOS soil moisture. *International Journal of Applied Earth Observation and Geoinformation*, *48*, 146–162. https://doi.org/10.1016/j.jag.2015.09.012

Martens, B., Miralles, D. G., Lievens, H., van der Schalie, R., de Jeu, R. A. M., Fernandez-Prieto, D., et al. (2017). GLEAM v3: Satellite-based land evaporation and root-zone soil moisture. *Geoscientific Model Development*, *10*(5), 1903–1925. https://doi.org/10.5194/gmd-10-1903-2017

Miao, X., Guo, W., Qiu, B., Lu, S., Zhang, Y., Xue, Y., & Sun, S. (2022). Accounting for topographic effects on snow cover fraction and surface albedo simulations over the Tibetan Plateau in winter. *Journal of Advances in Modeling Earth Systems*, *14*(8), e2022MS003035. https://doi.org/10.1029/2022MS003035

Miralles, D. G., Holmes, T. R. H., De Jeu, R. A. M., Gash, J. H., Meesters, A. G. C. A., & Dolman, A. J. (2011). Global land-surface evaporation estimated from satellite-based observations. *Hydrology and Earth System Sciences*, *15*(2), 453–469. https://doi.org/10.5194/hess-15-453-2011

Muller, M. D., & Scherer, D. (2005). A grid- and subgrid-scale radiation parameterization of topographic effects for mesoscale weather forecast models. *Monthly Weather Review*, *133*(6), 1431–1442. https://doi.org/10.1175/mwr2927.1

Nian, G. (2020). Effects of a 3-D terrain-based radiation scheme on land-air interactions over the Tibetan plateau: A land surface modelling study. *Atmospheric and Oceanic Science Letters*.

Oliphant, A. J., Spronken-Smith, R. A., Sturman, A. P., & Owens, I. F. (2003). Spatial variability of surface radiation fluxes in mountainous terrain. *Journal of Applied Meteorology*, *42*(1), 113–128. https://doi.org/10.1175/1520-0450(2003)042<0113:Svosrf>2.0.Co;2

Qiu, B., Huang, A., Shi, X., Dai, Y., Wei, N., Guo, W., et al. (2020). Implementation and evaluation of an improved lake scheme in Beijing climate center atmosphere-vegetation interaction model. *Journal of Geophysical Research: Atmospheres*, *125*(9). https://doi.org/10.1029/2019JD031272

Ruiz-Arias, J. A., Cebecauer, T., Tovar-Pescador, J., & Suri, M. (2010). Spatial disaggregation of satellite-derived irradiance using a high-resolution digital elevation model. *Solar Energy*, *84*(9), 1644–1657. https://doi.org/10.1016/j.solener.2010.06.002

Ruiz-Arias, J. A., Pozo-Vazquez, D., Lara-Fanego, V., Santos-Alamillos, F. J., & Tovar-Pescador, J. (2011). A high-resolution topographic correction method for clear-sky solar irradiance derived with a numerical weather prediction model. *Journal of Applied Meteorology and Climatology*, *50*(12), 2460–2472. https://doi.org/10.1175/2011jamc2571.1

Ruiz-Arias, J. A., Tovar-Pescador, J., Pozo-Vazquez, D., & Alsamamra, H. (2009). A comparative analysis of DEM-based models to estimate the solar radiation in mountainous terrain. *International Journal of Geographical Information Science*, *23*(8), 1049–1076. https://doi.org/10.1080/13658810802022806

Senkova, A. V., Rontu, L., & Savijarvi, H. (2007). Parametrization of orographic effects on surface radiation in HIRLAM. *Tellus A*, *59*(3), 279–291. https://doi.org/10.1111/j.1600-0870.2007.00235.x

Shen, Y., & Hu, J. (2006). Slope irradiance scheme in GRAPES and its effect on simulation of short-range weather processes. *Chinese Journal of Atmospheric Sciences*, *30*(6), 1129–1137.

Song, Y., Guo, W., & Zhang, Y. (2008). Simulation of latent heat flux exchange between land surface and atmosphere in temperate mixed forest and subtropical artificial coniferous forest sites in China by CoLM. *Plateau Meteorology*, *27*(5), 967–977.

Tang, B., Li, Z.-L., & Zhang, R. (2006). A direct method for estimating net surface shortwave radiation from MODIS data. *Remote Sensing of Environment*, *103*(1), 115–126. https://doi.org/10.1016/j.rse.2006.04.008

Tang, W., Yang, K., He, J., & Qin, J. (2010). Quality control and estimation of global solar radiation in China. *Solar Energy*, *84*(3), 466–475. https://doi.org/10.1016/j.solener.2010.01.006

Taylor, K. E. (2001). Summarizing multiple aspects of model performance in a single diagram. *Journal of Geophysical Research*, *106*(D7), 7183–7192. https://doi.org/10.1029/2000jd900719

Vignola, F., Harlan, P., Perez, R., & Kiniecik, M. (2007). Analysis of satellite derived beam and global solar radiation data. *Solar Energy*, *81*(6), 768–772. https://doi.org/10.1016/j.solener.2006.10.003

Wang, Q., Tenhunen, J., Schmidt, M., Otieno, D., Kolcun, O., & Droesler, M. (2005). Diffuse PAR irradiance under clear skies in complex alpine terrain. *Agricultural and Forest Meteorology*, *128*(1–2), 1–15. https://doi.org/10.1016/j.agrformet.2004.09.004

Wang, T., Yan, G., Mu, X., Jiao, Z., Chen, L., & Chu, Q. (2018). Toward operational shortwave radiation modeling and retrieval over rugged terrain. *Remote Sensing of Environment*, *205*, 419–433. https://doi.org/10.1016/j.rse.2017.11.006

Wang, X., Xie, H., Liang, T., & Huang, X. (2009). Comparison and validation of MODIS standard and new combination of Terra and Aqua snow cover products in northern Xinjiang, China. *Hydrological Processes*, *23*(3), 419–429. https://doi.org/10.1002/hyp.7151

Wood, S. W., Murphy, B. P., & Bowman, D. M. J. S. (2011). Firescape ecology: How topography determines the contrasting distribution of fire and rain forest in the south-west of the Tasmanian wilderness World Heritage Area. *Journal of Biogeography*, *38*(9), 1807–1820. https://doi.org/10.1111/j.1365-2699.2011.02524.x

Wu, G. X., Liu, Y. M., He, B., Bao, Q., Duan, A. M., & Jin, F. F. (2012). Thermal controls on the Asian summer monsoon. *Scientific Reports*, *2*(1), 404. https://doi.org/10.1038/srep00404

Wu, S., Wen, J., You, D., Zhang, H., Xiao, Q., & Liu, Q. (2018). Algorithms for calculating topographic parameters and their uncertainties in downward surface solar radiation (DSSR) estimation. *IEEE Geoscience and Remote Sensing Letters*, *15*(8), 1149–1153. https://doi.org/10.1109/lgrs.2018.2831916

Wu, Y., Huang, A. N., Huang, D. Q., Chen, F., Yang, B., Zhou, Y., et al. (2018). Diurnal variations of summer precipitation over the regions east to Tibetan Plateau. *Climate Dynamics*, *51*(11–12), 4287–4307. https://doi.org/10.1007/s00382-017-4042-x

Xian, Y., Wang, T., Cheng, W., Letu, H., Du, Y., & Leng, W. (2023). A uniform model for correcting shortwave downward radiation over rugged terrain at various scales. *IEEE Transactions on Geoscience and Remote Sensing*, *61*, 1–12. https://doi.org/10.1109/TGRS.2023.3278081

Xie, H., Wang, X., & Liang, T. (2009). Development and assessment of combined Terra and Aqua snow cover products in Colorado Plateau, USA and northern Xinjiang, China. *Journal of Applied Remote Sensing*, *3*(1), 033559. https://doi.org/10.1117/1.3265996

Xin, Y., Bian, L., & Zhang, X. (2006). The application of CoLM to arid region of Northwest China and Qinghai-Xizang Plateau. *Plateau Meteorology*, *25*(4), 567–574.

Xu, C. Y., & Singh, V. P. (2005). Evaluation of three complementary relationship evapotranspiration models by water balance approach to estimate actual regional evapotranspiration in different climatic regions. *Journal of Hydrology*, *308*(1–4), 105–121. https://doi.org/10.1016/j.jhydrol.2004.10.024

Xue, H., Zhou, X., Luo, Y., & Yin, J. (2021). Impact of parameterizing the turbulent orographic form drag on convection-permitting simulations of winds and precipitation over south China during the 2019 pre-summer rainy season. *Atmospheric Research*, *263*, 105814. https://doi.org/10.1016/j.atmosres.2021.105814

Yan, G., Jiao, Z.-H., Wang, T., & Mu, X. (2020). Modeling surface longwave radiation over high-relief terrain. *Remote Sensing of Environment*, *237*, 111556. https://doi.org/10.1016/j.rse.2019.111556

Yan, G., Wang, T., Jiao, Z.-H., Mu, X., Zhao, J., & Chen, L. (2016). Topographic radiation modeling and spatial scaling of clear-sky land surface longwave radiation over rugged terrain. *Remote Sensing of Environment*, *172*, 0034–4257. https://doi.org/10.1016/j.rse.2015.10.026

Yang, K., He, J., Tang, W., Lu, H., Qin, J., Chen, Y., & Li, X. (2019). China meteorological forcing dataset (1979-2018) [Dataset]. *A Big Earth Data Platform for Three Poles*. https://doi.org/10.11888/AtmosphericPhysics.tpe.249369.file

Yang, K., He, J., Tang, W. J., Qin, J., & Cheng, C. (2010). On downward shortwave and longwave radiations over high altitude regions: Observation and modeling in the Tibetan Plateau. *Agricultural and Forest Meteorology*, *150*(1), 38–46. https://doi.org/10.1016/j.agrformet.2009.08.004

Yang, W., Ye, D., & Wu, G. X. (1992). The influence of the Tibetan Plateau on the thermal and circulation fields over East Asia in summer. II: Main features of the local and large-scale vertical circulation fields. *Chinese Journal of Atmospheric Sciences*, *16*, 287–301.

Ye, D. Z. (1980). Some characteristics of the summer circulation over the Qinghai-Xizang (Tibet) Plateau and its neighborhood. *Bulletin of the American Meteorological Society*, *62*(1), 14–19. https://doi.org/10.1175/1520-0477(1981)062<0014:SCOTSC>2.0.CO;2

Yuan, H., Dai, Y., Dickinson, R., Pinty, B., Shangguan, W., Zhang, S., et al. (2016). Reexamination and further development of two-stream canopy radiative transfer models for global land modeling. *Journal of Advances in Modeling Earth Systems*, *9*(1), 113–129. https://doi.org/10.1002/2016MS000773

Zhang, W., Huang, A. N., Zhou, Y., Yang, B., Fang, D. X., Zhang, L. J., & Wu, Y. (2017). Diurnal cycle of precipitation over Fujian Province during the pre-summer rainy season in southern China. *Theoretical and Applied Climatology*, *130*(3–4), 993–1006. https://doi.org/10.1007/s00704-016-1927-2

Zhang, X., Huang, A., Dai, Y., Li, W., Gu, C., Yuan, H., et al. (2022). Influences of 3D sub-grid terrain radiative effect on the performance of CoLM over Heihe River Basin, Tibetan Plateau. *Journal of Advances in Modeling Earth Systems*, *14*(1), e2021MS002654. https://doi.org/10.1029/2021MS002654

Zhang, X., & Liang, S. (2018). The global LAnd surface satellite (GLASS) 0.05Deg daily DSR product [Dataset]. *National Earth System Science Data Center*. https://doi.org/10.12041/geodata.GLASS_DSR_modis(0.05D).ver1.db

Zhang, X., Liang, S., Song, Z., Niu, H., Wang, G., Tang, W., et al. (2016). Local adaptive calibration of the satellite-derived surface incident shortwave radiation product using smoothing spline. *IEEE Transactions on Geoscience and Remote Sensing*, *54*(2), 1156–1169. https://doi.org/10.1109/tgrs.2015.2475615

Zhang, X., Liang, S., Zhou, G., Wu, H., & Zhao, X. (2014). Generating Global LAnd Surface Satellite incident shortwave radiation and photosynthetically active radiation products from multiple satellite data. *Remote Sensing of Environment*, *152*, 318–332. https://doi.org/10.1016/j.rse.2014.07.003

Zhang, X., Liu, L. Y., Chen, X. D., Xie, S., & Gao, Y. (2019). Fine land-cover mapping in China using landsat datacube and an operational SPECLib-based approach. *Remote Sensing*, *11*(9), 1056. https://doi.org/10.3390/rs11091056

Zhang, X., Wang, D., Liu, Q., Yao, Y., & Liang, S. (2019). An operational approach for generating the global land surface downward shortwave radiation product from MODIS data. *IEEE Transactions on Geoscience and Remote Sensing*, *PP*(99), 1–15. https://doi.org/10.1109/TGRS.2019.2891945

Zhang, Y., Huang, A., & Zhu, X. (2006). Parameterization of the thermal impacts of sub-grid orography on numerical modeling of the surface energy budget over East Asia. *Theoretical and Applied Climatology*, *86*(1–4), 201–214. https://doi.org/10.1007/s00704-005-0209-1

Zhang, Y. L., Li, X., Cheng, G. D., Jin, H. J., Yang, D. W., Flerchinger, G. N., et al. (2018). Influences of topographic shadows on the thermal and hydrological processes in a cold region mountainous watershed in Northwest China. *Journal of Advances in Modeling Earth Systems*, *10*(7), 1439–1457. https://doi.org/10.1029/2017ms001264

Zhao, B., Mao, K., Cai, Y., Shi, J., Li, Z., Qin, Z., & Meng, X. (2019). A combined Terra and Aqua MODIS land surface temperature and meteorological station data product for China from 2003–2017 (version 1.1) [Dataset]. *Zenodo*. https://doi.org/10.5281/zenodo.3528024

Zhao, B., Mao, K., Cai, Y., Shi, J., Li, Z., Qin, Z., et al. (2020). A combined Terra and Aqua MODIS land surface temperature and meteorological station data product for China from 2003 to 2017. *Earth System Science Data*, *12*(4), 2555–2577. https://doi.org/10.5194/essd-12-2555-2020

Zheng, J., Xie, Z., & Dai, Y. (2009). Coupling of the Common Land Model (CoLM) with the Regional Climate model (RegCM3) and its preliminary validation. *Chinese Journal of Atmospheric Sciences*, *33*(4), 737–750. https://doi.org/10.3878/j.issn.1006-9895.2009.04.08

Zhong, S., & Chen, Z. (2015). Improved wind and precipitation forecasts over South China using a modified orographic drag parameterization scheme. *Journal of Meteorological Research*, *29*(1), 132–143. https://doi.org/10.1007/s13351-014-4934-1

Zhou, M., W, Y. L. H., et al. (2019). Comparative analysis of the snow coverage products of Soumi-NPP and MODIS in the Qinghai-Tibet Plateau (in Chinese). *Journal of Glaciology and Geocryology*, *41*(1), 36–44. https://doi.org/10.7522/j.issn.1000-0240.2018.0320

Zhou, X., Yang, K., Beljaars, A., Li, H., Lin, C., Huang, B., & Wang, Y. (2019). Dynamical impact of parameterized turbulent orographic form drag on the simulation of winter precipitation over the western Tibetan Plateau. *Climate Dynamics*, *53*(1–2), 707–720. https://doi.org/10.1007/s00382-019-04628-0